How to cite: *Angew. Chem. Int. Ed.* **2024**, *63*, e202306033
doi.org/10.1002/anie.202306033

Polymerization Catalysis

Visualizing the Structure, Composition and Activity of Single Catalyst Particles for Olefin Polymerization and Polyolefin Decomposition

Maximilian J. Werny, Florian Meirer, and Bert M. Weckhuysen**

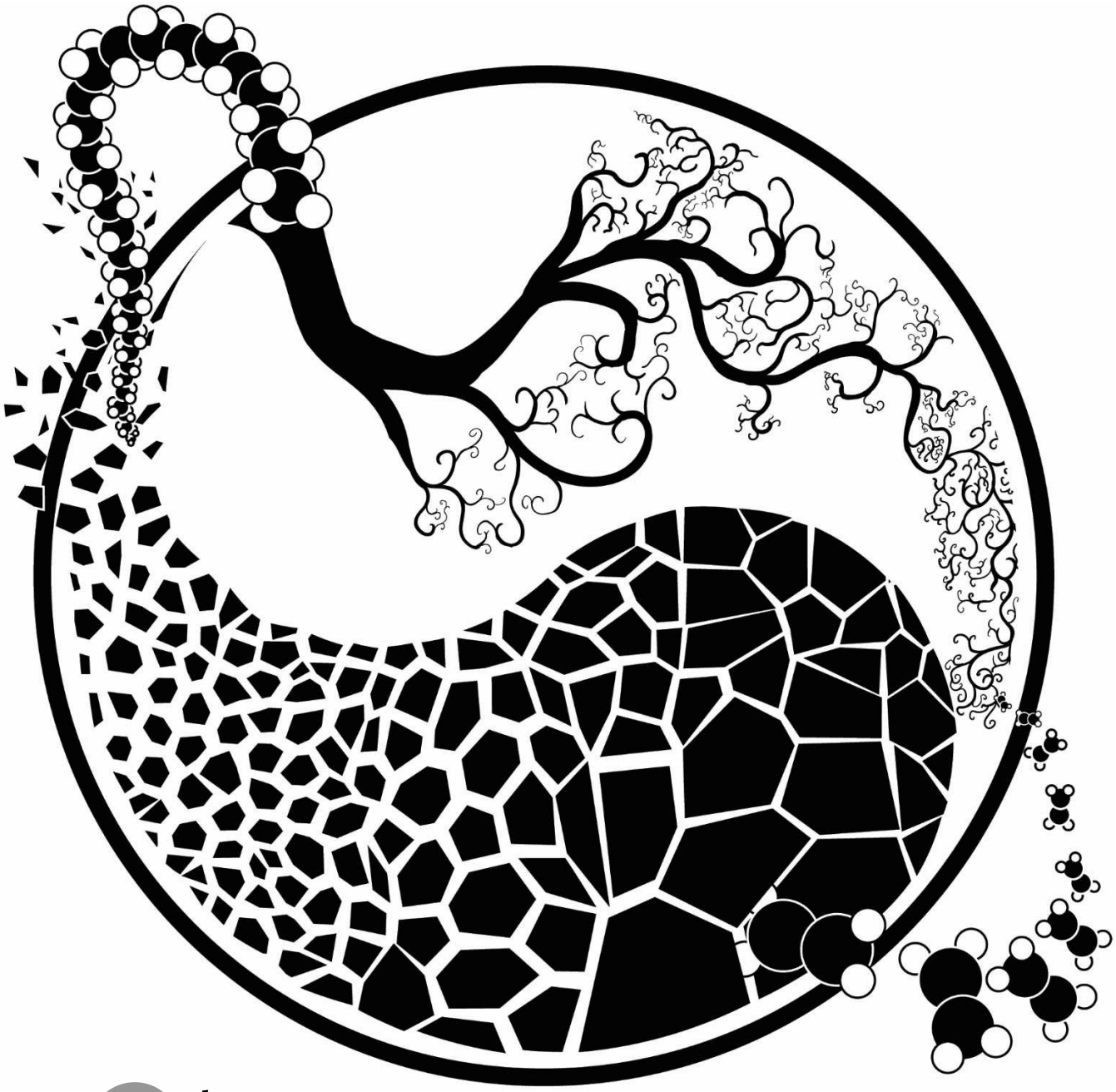

Angewandte International Edition Chemie

Abstract: The structural and morphological characterization of individual catalyst particles for olefin polymerization, as well as for the reverse process of polyolefin decomposition, can provide an improved understanding for how these catalyst materials operate under relevant reaction conditions. In this review, we discuss an emerging analytical toolbox of 2D and 3D chemical imaging techniques that is suitable for investigating the chemistry and reactivity of related catalyst systems. While synchrotron-based X-ray microscopy still provides unparalleled spatial resolutions in 2D and 3D, a number of laboratory-based techniques, most notably focused ion beam-scanning electron microscopy, confocal fluorescence microscopy, infrared photoinduced force microscopy and laboratory-based X-ray nano-computed tomography, have helped to significantly expand the arsenal of analytical tools available to scientists in heterogeneous catalysis and polymer science. In terms of future research, the review outlines the role and impact of in situ and operando (spectro−)microscopy experiments, involving sophisticated reactors as well as online reactant and product analysis, to obtain real-time information on the formation, decomposition, and mobility of polymer phases within single catalyst particles. Furthermore, the potential of fluorescence microscopy, X-ray microscopy and optical microscopy is highlighted for the high-throughput characterization of olefin polymerization and polyolefin decomposition catalysts. By combining these chemical imaging techniques with, for example, chemical staining methodologies, selective probe molecules as well as particle sorting approaches, representative structure–activity relationships can be derived at the level of single catalyst particles.

1. Introduction

Over the past century, the polyolefin industry has grown steadily.[1,2] In fact, polyolefin resins accounted for 45 % of the total polymer production in 2017.[3] Polyolefins are widely used in our day-to-day lives due to their advantageous physical, chemical, and mechanical properties. The insufficient recycling of these materials as well as their uncontrolled release into the environment,[1] however, represent pressing problems and require immediate attention.

From a historical point of view, industrial olefin polymerization has its roots in the 1930s.[4] It was in this period that ethylene was first polymerized to form low-density polyethylene (LDPE) via a high-temperature and high-pressure radical process. In the 1950s, two families of heterogeneous catalysts were discovered for olefin polymerization under milder conditions, i.e., the Phillips catalyst (e.g., CrO_x/SiO_2) and the Ziegler–Natta catalyst (e.g., $TiCl_4/MgCl_2$).[4] Until this very day, the two catalyst systems contribute largely to the production of various grades of high-density polyethylene (HDPE), linear low-density polyethylene (LLDPE), as well as polypropylene (PP).[5] Supported metallocene/MAO-based catalysts (with MAO = methylaluminoxane) were discovered in the 1980s and are well suited to producing specialty polymers with more complex microstructures and tacticities, such as isotactic PP (i-PP).[6,7]

In contrast to the rather mature field of catalytic olefin polymerization, the field of catalytic polyolefin recycling has only gained momentum in recent years. Processes, such as catalytic pyrolysis (i.e., thermal cracking), hydrocracking and hydrogenolysis, offer viable pathways to convert plastic waste into chemical building blocks, thus ensuring the circularity of these polymer materials.[8,9] The aim is to convert plastic waste into, for example, naphtha-like fractions for refining operations, fuels such as gasoline or diesel, and valuable monomers for the polyolefin industry (Figure 1A). By employing heterogeneous catalysts, such as zeolites, for the pyrolysis of polyolefins, such as PP, a mixture of alkanes and methyl-aromatics can be obtained at temperatures that are lower than those employed in non-catalytic pyrolysis.[10] In fact, affordable solid catalysts, such as fluid catalytic cracking (FCC) and related equilibrium FCC cracking (ECAT) catalysts, have been reported to convert PP into aliphatic and aromatic compounds, alkenes and propylene in the absence of hydrogen.[11] Supported metal nanoparticles (most commonly Pt, Ru, and Ni), metal oxides and zeolite catalysts, on the other hand, have shown promising performance in the hydrocracking and hydrogenolysis of HDPE, LDPE, and mixed plastic waste.[12–18]

Mechanistically speaking, polyolefins, such as PE or PP, are formed via insertion of ethylene or propylene into a M–H or M-alkyl bond, followed by multiple insertions of monomers into the resulting M-alkyl bond.[19–21] According to the principle of microkinetic reversibility, the olefin polymerization reaction can be reversed to yield olefinic monomers. This process of depolymerization, which essentially involves a β-alkyl elimination step, is thermodynamically unfavorable (i.e., endergonic, see potential energy diagram in Figure 1B).[22,23] In fact, the activation energies for the thermal decomposition of PE and PP have been reported to lie in the range of ~ 140–300 kJ/mol.[24] The hydrogenolysis of the olefin, however, results in the process of polymer chain scission becoming thermodynamically

[*] Dr. M. J. Werny, Dr. F. Meirer, Prof. Dr. B. M. Weckhuysen
Inorganic Chemistry and Catalysis, Institute for Sustainable and Circular Chemistry and Debye Institute for Nanomaterials Science, Utrecht University, Universiteitsweg 99, 3584 CG Utrecht (The Netherlands)
E-mail: f.meirer@uu.nl
b.m.weckhuysen@uu.nl
Dr. M. J. Werny
Dutch Polymer Institute (DPI), P.O. Box 902, 5600 AX Eindhoven (The Netherlands)

accessible (Figure 1B).[20,23,25,26] This was validated in 1988 by Dufaud and Basset, who reported on a supported Ziegler–Natta-type zirconium hydride catalyst that not only formed PE, but also cleaved the same molecule in the presence of hydrogen at 150 °C.[20]

Having explored this mechanistic correlation between olefin polymerization and depolymerization, it is also of interest to consider the physicochemical properties of the heterogeneous catalyst systems under reaction conditions. While significant mass transfer limitations arise during olefin polymerization due to a rapid build-up of polymer in the pores of the catalyst support,[27,28] mass transfer is similarly limited when molten polymer enters the macropores of a catalyst particle during a polyolefin decomposition reaction. It is thus clearly evident that the spatial distribution of the polymer phase, and, in the case of polyolefin cracking, its mobility and decomposition, critically influence the reactivity of a catalyst particle. In order to make definitive conclusions about these dynamic processes, imaging techniques with high spatial and temporal resolutions are necessary. These can deliver information on the morphology of individual particles (Figure 1C) at the nanometer scale, thus helping to identify and define structure–activity relationships.

Single particle data can generally help to rationalize trends derived from bulk catalytic testing. Similarly important, however, is the identification of particles with atypical or unexpected reactivities, structures and compositions. Considering the large degrees of interparticle heterogeneity that are observed in pristine industrial catalysts,[29–31] investigations into a representative number of individual particles at high spatial resolutions, preferably in 3D, are vital to fully understand their structural and chemical complexity. This becomes even more relevant when considering the lifetime of a catalyst inside a chemical reactor, where concentration and temperature gradients, and, in certain cases, dynamic reactor operations (e.g., fluidized bed reactors, stirred tank reactors, loop reactors, etc.) result in varying reaction conditions and residence times for individual catalyst particles. This affects their reactivity, composition and morphology.

In the past, various characterization techniques have been successfully used to visualize and understand the structural evolution of industrially relevant olefin polymerization catalysts. In this review, we provide an overview of these state-of-the-art analytical techniques and will highlight their potential for studying structural and compositional changes in olefin polymerization and the reverse process of catalytic plastic decomposition/cracking (Table 1). Both laboratory- and synchrotron-based techniques can deliver information on the structure, composition and reactivity of relevant heterogeneous catalysts at the single particle level. Such insights are vital for a better understanding of the

Maximilian J. Werny graduated in 2018 with a M.Sc. in Inorganic Chemistry and Catalysis from the Technical University of Munich (TUM, Germany). Since then, he has been investigating structure–activity-morphology relationships in industrial-grade olefin polymerization catalysts in the group of Prof. Bert Weckhuysen (Utrecht University, The Netherlands) using advanced microscopy and spectroscopy techniques. His research is funded by the Dutch Polymer Institute (DPI, Eindhoven, The Netherlands) and involves collaborations with several research groups in Italy and Germany. He recently obtained his PhD degree from Utrecht University.

Florian Meirer obtained his ScD degree (2008) in technical physics from the TU Wien (Vienna University of Technology, Prof. Christina Streli). After postdoctoral stays at the Stanford Synchrotron Radiation Lightsource, USA, (Prof. Piero Pianetta) and the Fondazione Bruno Kessler, Italy (Marie-Curie cofund fellowship), he moved to Utrecht University to work on spectroscopic and spectro-microscopic methods for the characterization of solid catalysts and related nanomaterials. He is currently Associate Professor and his fields of research include spectro-microscopy, data mining, and chemometrics in the fields of heterogeneous catalysis and environmental analysis.

Bert M. Weckhuysen obtained his PhD degree from KU Leuven (Belgium, with Prof. Robert Schoonheydt) in 1995. After postdoctoral stays at Lehigh University (PA, USA, with Prof. Israel Wachs) and Texas A&M University (TX, USA, with Prof. Jack Lunsford), he became a full Professor at Utrecht University (The Netherlands) in 2000. His research focuses on the development and use of in situ and operando spectroscopy for studying solid catalysts under both realistic reaction conditions and at different length scales. The aim is to understand reaction and deactivation mechanisms in heterogeneous catalysts that convert renewable (agricultural and municipal waste, as well as carbon dioxide) and non-renewable (methane and crude oil) resources to fuels, chemicals and materials.

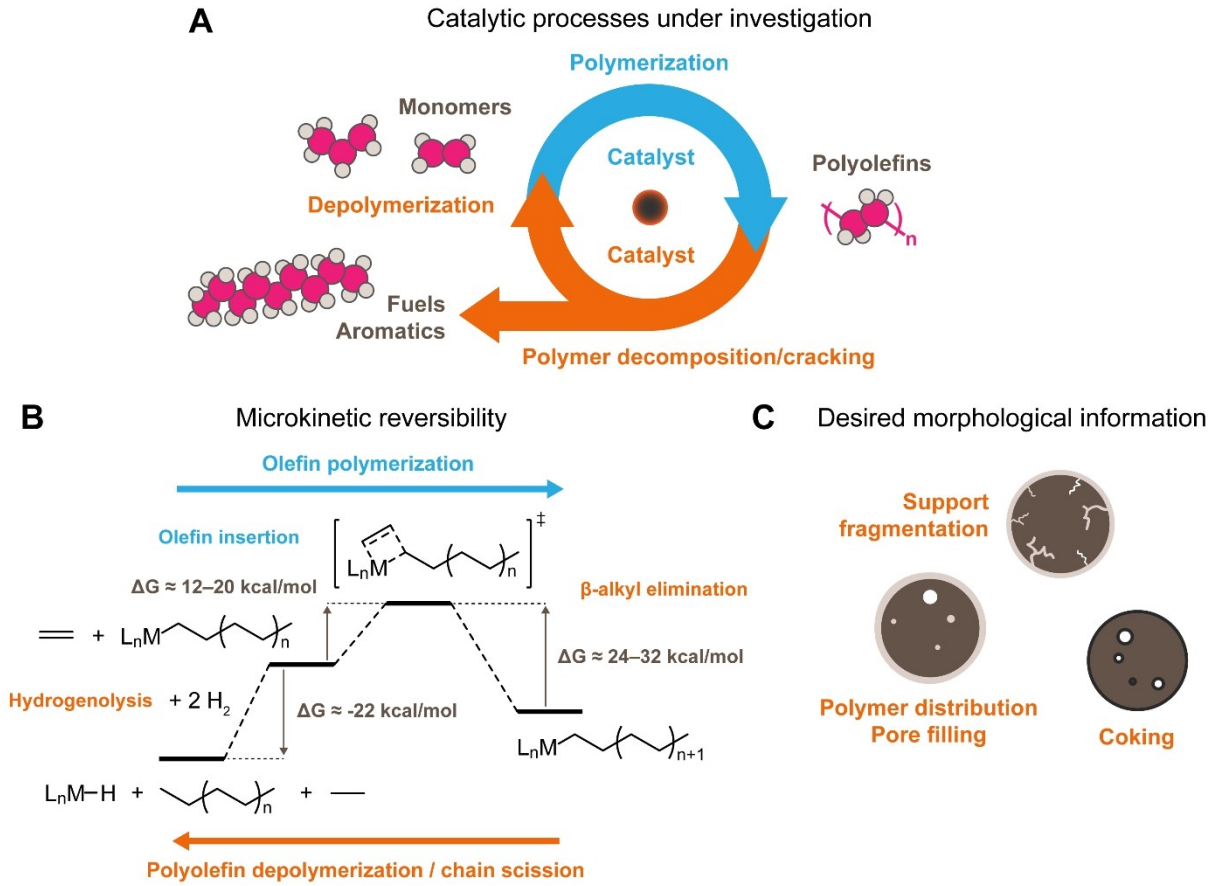

Figure 1. A: Catalyst-mediated circularity in the polyolefins value chain. Polyolefins can be decomposed or cracked in the presence of a catalyst to yield fuels and aromatics, or depolymerized catalytically to form the chemical building blocks (i.e., monomers) that they have been synthesized from. B: Potential energy diagram for the processes of olefin insertion (i.e., polymerization), β-alkyl elimination (i.e., depolymerization) and hydrogenolysis. Reproduced and adapted from ref. [23]. Copyright © 2022 Wiley-VCH, published by John Wiley and Sons. C: Main insights that can be extracted with 2D and 3D chemical imaging techniques from heterogeneous catalysts employed in olefin polymerization and polymer decomposition/cracking reactions.

catalysts, mass transport and reaction pathways, and can ultimately advance the design of novel catalyst materials.

2. Assessing the morphology and activity of supported olefin polymerization catalyst particles

Conventional polyolefins, such as PE and PP, are solid materials that are formed via polymerization of their respective monomers, i.e., ethylene, propylene and, depending on the PE grade, different co-monomers such as 1-butene, 1-hexene or 1-octene. As mentioned above, the production of HDPE, LLDPE and PP is dominated by various transition metal-based catalysts on inorganic supports, such as silica or magnesium chloride. Once these polymers are formed inside the pores of a given catalyst support, stress is generated. When this stress crosses a certain threshold, as is, amongst others, determined by the mechanical stability of the support material, the support begins to break apart. This physical disintegration of the catalyst support is referred to as fragmentation. Fragmentation plays a central role in the morphological development of olefin polymerization catalyst particles. Under ideal conditions, each spherical catalyst particle in the size range of 10–100 μm disintegrates uniformly during polymerization to form a 100–3000 μm sized polymer particle with the same shape as the initial catalyst support. The catalyst support remains highly dispersed in the formed polymer matrix. This is known as the replica effect.[32] An incomplete fragmentation of the support can lead to residual support fragments in the formed polymer, often affecting its quality, and lower the total polymer yield. Uncontrolled or very rapid fragmentation, on the other hand, can result in the break-off of smaller support fragments, which continue to fragment and polymerize as separate entities. These so-called 'fines' are known to affect the physico-chemical properties of the polymer and can also cause reactor fouling.

Two mechanisms of catalyst particle fragmentation, namely, the layer-by-layer and the sectioning mechanism, have been widely reported in literature.[33–36] It is the synergy of both mechanisms that ultimately guarantees uniform particle growth and a high dispersion of the catalyst in the formed polymer matrix.[37,38] In the layer-by-layer mecha-

Table 1: Overview of 2D and 3D imaging techniques with sub-micron spatial resolutions that have been applied to olefin polymerization or polyolefin decomposition/cracking catalyst particles (including cross-sections thereof). The 2D resolutions correspond to resolutions in the xy-plane, and are approximated values, only meant to provide relative comparisons between the different imaging techniques.

Characterization technique	Typical samples/measurement regions	Advantages	Disadvantages
Scanning electron microscopy (SEM)	Individual or multiple catalyst particles/particle cross-sections in 2D	High 2D spatial resolutions ($\sim 10^1$ nm), laboratory-based technique, short measurement times, no image reconstruction algorithms required, element-specific imaging if combined with energy-dispersive X-ray spectroscopy (EDX)	Very time-intensive 3D imaging (slice and view), elaborate and destructive sample preparation required for imaging particle cross-sections (focused ion beam milling or microtoming), XRF data acquired with EDX is difficult to quantify and not representative of bulk materials
Scanning transmission electron microscopy (STEM)	Microtomed catalyst particle cross-section in 2D, typical measurement areas: $< 10^2$ μm^2	Very high 2D spatial resolutions ($\sim 10^{-1}$–10^0 nm), laboratory-based technique, short measurement times, no image reconstruction algorithms required, element-specific imaging if combined with energy-dispersive X-ray spectroscopy (EDX)	Non-representative of complex composite materials, elaborate and destructive sample preparation required for imaging particle cross-sections (microtoming), very time-intensive 3D imaging
Atomic force microscopy (AFM)	Individual catalyst particle/planar catalyst surface or particle cross-section, typical measurement areas: $< 10^2$ μm^2	Very high 2D spatial resolutions ($\sim 10^0$–10^1 nm), laboratory-based technique, short-medium measurement times, topological information, no image reconstruction algorithms required	Only 2D imaging, small scan area, flat samples required, non-representative of complex composite materials, elaborate and destructive sample preparation required for imaging particle cross-sections (FIB/microtoming)
Infrared photoinduced force microscopy (IR PiFM)	Individual catalyst particle/planar catalyst surface or particle cross-section, typical measurement areas: $< 10^2$ μm^2	High 2D spatial resolutions ($\sim 10^1$ nm), laboratory-based technique, short-medium measurement times, material identification via IR nano-spectroscopy, topological information via AFM, mechanical properties via phase imaging, no image reconstruction algorithms required	Only 2D imaging, small scan area, flat samples required, non-representative of complex composite materials, elaborate and destructive sample preparation required for imaging particle cross-sections (FIB/microtoming)
Raman microscopy (RM)	Individual particle/particle cross-section in 2D	Short-medium measurement times, laboratory-based technique, relatively non-destructive, no image reconstruction algorithms required, 3D imaging via confocal Raman microscopy	Low-moderate 2D spatial resolutions ($\sim 10^2$–10^3 nm), beam damage possible
Confocal fluorescence microscopy (CFM)	Individual or multiple particles/particle cross-sections in 2D and 3D	High sample throughput (both in 2D/3D), short measurement times, laboratory-based technique, non-destructive, no image reconstruction algorithms required	Moderate 2D spatial resolutions ($\sim 10^2$–10^3 nm), scattering and absorption impede characterization of larger catalyst particles (i.e., only sub-volumes can be measured)
Single-molecule fluorescence (SMF) microscopy	Individual catalyst particle in 2D	Short-medium measurement times, laboratory-based technique, non-destructive, no image reconstruction algorithms required	High 2D spatial resolutions ($\sim 10^1$–10^2 nm), limited to 2D, may require the use of fluorescent model compounds instead of actual reactants, elaborate data analysis
Scanning X-ray transmission microscopy (STXM, soft X-rays)	Microtomed particle cross-section in 2D	Very high 2D spatial resolutions ($\sim 10^1$ nm), chemical imaging, including oxidation states, relatively non-destructive	2D imaging and in principle 3D imaging possible, small scan area, synchrotron-based technique, capital intensive, thin samples required (<1 μm), elaborate data analysis
Nano-computed tomography (nanoCT)	Individual or multiple particles in 3D	High 3D spatial resolutions ($\sim 10^2$ nm), relatively non-destructive, laboratory-based technique (more accessible than synchrotron-based X-ray microscopy)	Medium-long measurement times, low-medium sample throughput, capital intensive, elaborate image reconstruction and data analysis
Ptychographic X-ray computed tomography (PXCT)	Individual or multiple particles in 3D	Very high 3D spatial resolutions ($\sim 10^1$–10^2 nm), yields quantitative data on electron density, relatively non-destructive	Long measurement times and low sample throughput with a single beam (not applicable for multibeam operation), synchrotron-based technique, capital intensive, elaborate image reconstruction and data analysis
X-ray fluorescence (XRF) tomography	Individual or multiple particles in 3D	Element-specific 3D imaging, relatively non-destructive, yields quantitative data	Long measurement times, low sample throughput, moderate 3D spatial resolutions ($\sim 10^2$–10^3 nm), synchrotron-based technique, capital intensive, elaborate image reconstruction and data analysis
Holotomography (HT)	Individual or multiple particles in 3D	High sample throughput, high 3D spatial resolutions ($\sim 10^2$ nm), short measurement times, relatively non-destructive	Synchrotron-based technique, capital intensive, elaborate image reconstruction and data analysis

nism, polymerization and fragmentation start at the surface of the catalyst particle or its constituent support granulates, resulting in their gradual disintegration from the surface towards their respective cores (Figure 2A). In the sectioning mechanism, the formation of large, extensive cracks results in the cleavage of the support granulates, or, in some cases, of the entire catalyst particle into multiple larger fragments (Figures 2B and 2 C). The fragmentation of the support is generally more uncontrolled and can lead to a fast exposure of active sites deep within the catalyst particle. The contribution of either mechanism is dictated by the properties of the catalyst support (i.e., surface area, porosity, pore size distribution, particle size and mechanical rigidity), the actives sites (distribution, structure, activity and accessibility), the type of α-olefin monomer, the crystallinity of the formed polymer, the process conditions (i.e., temperature, pressure, reaction phase, stirring rate, catalyst bed fluidization, co-catalyst type, and concentration), as well as heat transfer and mass transfer, which are strongly related to the operating conditions.[27,28,39] The large number of experimental variables creates significant complexity when attempting to identify factors that are largely responsible for a given catalyst particle morphology. In addition to this, the considerable speed of the fragmentation process under industrial conditions currently impedes any true in situ characterization of catalyst particles.

In the following sections, leading analytical techniques for the 2D and 3D assessment of olefin polymerization catalyst particle morphologies and activities will be outlined. The here discussed morphological investigations were predominantly performed ex situ on pristine and pre-polymerized catalyst samples.

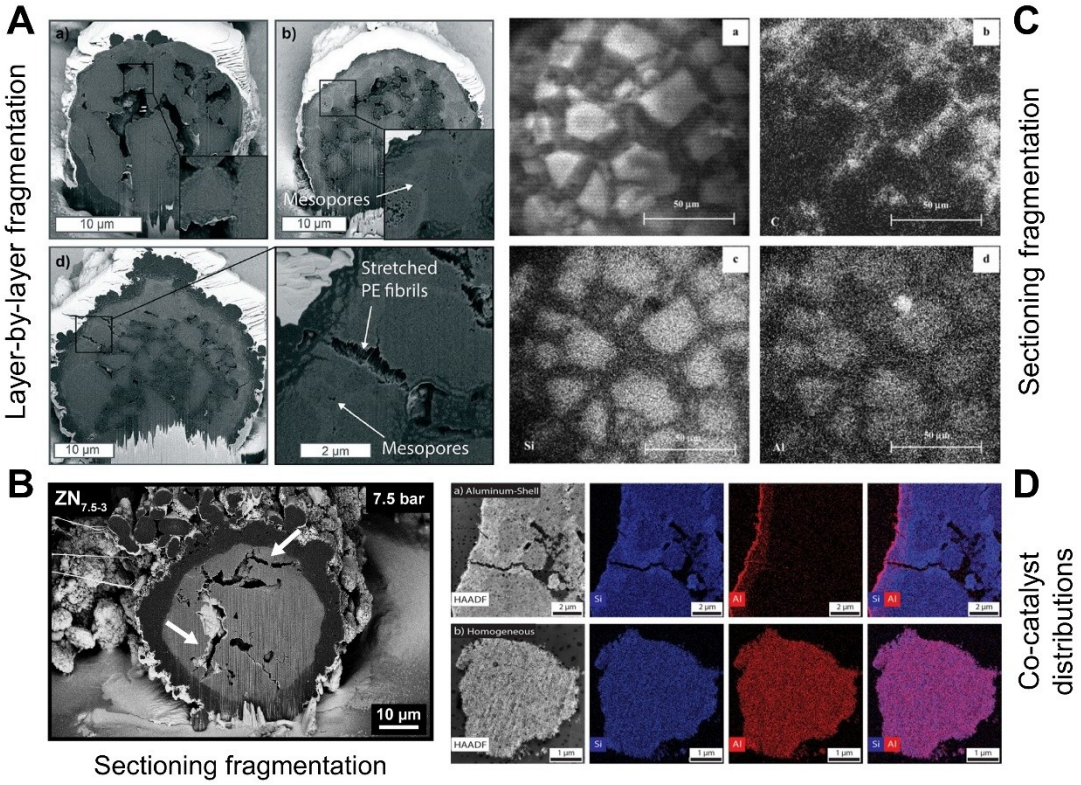

Figure 2. Examples of morphological and chemical information that can be extracted with different electron microscopy techniques. A: Focused ion beam-scanning electron microscopy (FIB-SEM) cross-sectional images of silica-supported metallocene-based catalyst particles pre-polymerized in gas-phase at 1 bar ethylene pressure and room temperature for different periods of time. Light gray domains correspond to the silica support, while the dark gray domains represent polyethylene (PE). A strong manifestation of the layer-by-layer fragmentation mechanism is evident, both at the particle surface and at the exposed surfaces of the supports' constituent granulates. Reproduced and adapted from ref. [47] with permission from the Royal Society of Chemistry under the CC BY 3.0 license. The Figure is an excerpt of the original. B: FIB-SEM cross-sectional image of a silica-supported Ziegler–Natta (ZN) catalyst particle pre-polymerized for 1 min at 7.5 bar ethylene pressure and room temperature. The particle has fragmented following the sectioning fragmentation mechanism (indicated by white arrows). Reproduced and adapted from ref. [48] under the CC BY 4.0 license. The figure is an excerpt of the original. Copyright © 2022 Werny et al., published by Wiley-VCH. C: Scanning electron microscopy (SEM) image (top left) and energy-dispersive X-ray spectroscopy (EDX) maps (C: top right, Si: bottom left, and Al: bottom right) of a silica-supported metallocene catalyst particle after polymerization with propylene (1 h, 50 °C, 4 bar propylene pressure). The outer sphere of the particle has fragmented following the sectioning fragmentation mechanism. Reprinted (adapted) with permission from ref. [50]. Copyright © 2005, American Chemical Society. D: Scanning transmission electron microscopy-energy-dispersive X-ray spectroscopy (STEM-EDX) maps (Si: blue, Al: red) recorded of the microtomed cross-sections of two pristine silica-supported metallocene catalysts with Al/Zr molar ratios of 51 (top) and 132 (bottom). A distinct aluminum (Al) shell is observed in the sample with a lower Al loading, while the Al distribution is more homogeneous at higher loadings. Reproduced from ref. [29] under the CC BY-NC-ND 4.0 license. Copyright © 2018 Velthoen et al., published by Wiley-VCH Verlag.

2.1. Electron microscopy

Scanning electron microscopy (SEM) is one of the most commonly used methods to assess the morphology of supported polymerization catalyst particles[40–45] and can yield unparalleled 2D resolutions below 30 nm. It is generally used to determine both the external and internal morphology of individual particles. For the latter, the cross-sections of individual particles are accessed via microtoming or focused ion beam (FIB) cutting and are subsequently imaged. By adopting a horizontal FIB cutting approach,[38] complementary scanning probe techniques, such as infrared photoinduced force microscopy (IR PiFM, Figure 3) and atomic force microscopy-infrared spectroscopy (AFM-IR),

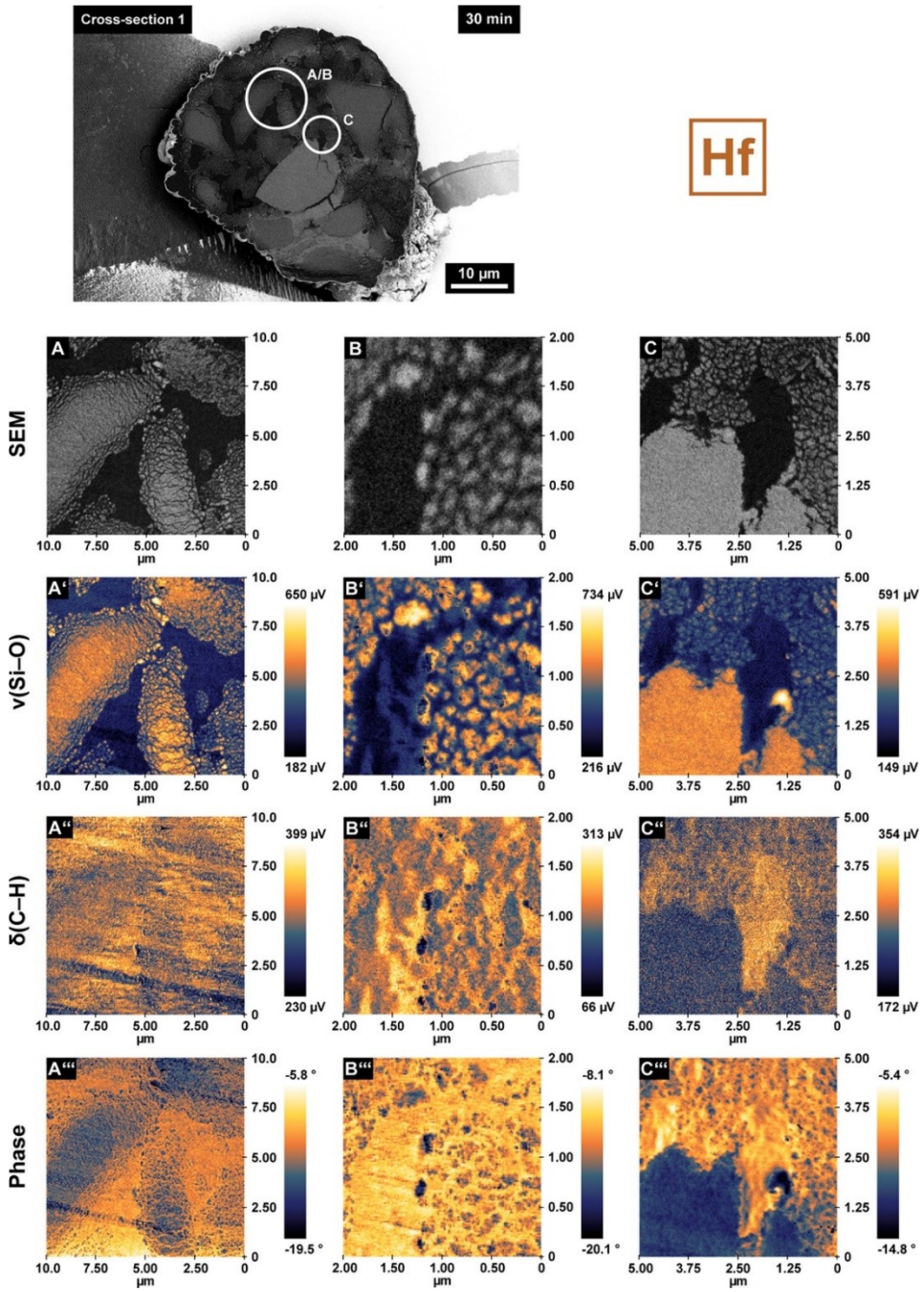

Figure 3. Scanning electron microscopy (SEM) and infrared photoinduced force microscopy (IR PiFM) data recorded on the horizontal cross-section of a silica-supported hafnocene (Hf = hafnocene/MAO/SiO_2 with MAO = methylaluminoxane) after ethylene pre-polymerization (30 min, room temperature, 1.6 bar ethylene pressure). With the help of IR PiFM, the distribution of different materials (e.g., silica, PE) in the composite particle can be verified spectroscopically [i.e., by recording IR maps at defined wavenumbers for ν(Si–O) and δ(C–H)] as well as mechanically (i.e., via phase imaging). Reproduced and adapted from ref. [38]. Copyright © 2021 Werny et al., published by American Chemical Society under the CC BY-NC-ND 4.0 license.

as well as vibrational microscopy techniques, such as IR or Raman microscopy, can be used to verify the distribution of different phases (e.g., silica, polymer, pores), either spectroscopically or topographically.[38,46] Together, these methods can help to assess the chemical composition, mechanical properties and crystallinities of nascent polymers at different reaction stages.[38,46]

In recent studies, SEM has been used to image and investigate the early stages of pre-polymerization and fragmentation in silica-supported metallocenes, both at low and high ethylene pressures.[38,47–49] Here, the particle cross-sections were imaged in backscattered electron (BSE) mode, thus yielding clear contrast between the polymer and the more electron dense silica fragments (Figure 2A). From a mechanistic point of view, the layer-by-layer mechanism was found to play a prominent role in the fragmentation of these catalyst systems. Contributions from the sectioning mechanism were only observed under more pronounced mass transfer limitations, often in domains of low macroporosity. A remarkably pronounced involvement of the sectioning mechanism was reported for a silica-supported Ziegler–Natta catalyst, which was investigated with FIB-SEM (Figure 2B) and nano-computed tomography (nanoCT). Extensive crack formation—associated with the fast kinetics of the Ziegler–Natta catalyst, a rapid formation of polyethylene and significant pressure build-up—led to the break-up of entire catalyst particle–particles in the early stages of slurry-phase ethylene polymerization.[48]

SEM instruments are usually equipped to perform energy-dispersive X-ray spectroscopy (EDX). This can be a useful complementary tool for determining the distribution of different catalyst components and reaction products (Figure 2C).[50,51] Velthoen et al. used SEM-EDX, along with scanning transmission electron microscopy-energy-dispersive X-ray spectroscopy (STEM-EDX, Figure 2D), to visualize and quantify compositional heterogeneities in silica-supported metallocene samples with different co-catalyst (methylaluminoxane, MAO) loadings.[29] The investigation of multiple particles helped to identify an optimal MAO loading at which the interparticle heterogeneity was sufficiently low. Tran et al. used a combination of FIB-SEM and energy-dispersive X-ray spectroscopy (EDX) to study the impact of the impregnation time and catalyst solution concentration on the radial distribution of a zirconocene complex in individual catalyst particle cross-sections, and the influence thereof on the catalyst particle morphology.[52] High metallocene concentrations in the peripheral regions of the particle were postulated to cause more fines in the final polymer product.

2.2. X-ray microscopy

X-ray microscopy is highly suitable for studying the structure and chemical composition of heterogeneous catalysts, often in 3D.[53,54] By relying on absorption or phase imaging contrast, catalyst components and products with different electron densities can be distinguished. Techniques such as scanning transmission X-ray microscopy (STXM, 2D, soft X-rays); transmission X-ray microscopy (TXM, 3D, hard X-rays) and X-ray fluorescence tomography (XRF, 3D) can even be used to determine the spatial distribution and chemical state of specific elements. In contrast to SEM, which requires the physical removal of a particle sub-volume for cross-sectional imaging, X-ray microscopy is generally considered to be relatively non-destructive.

In the field of olefin polymerization catalysts, the first efforts to image individual catalyst particles with hard X-rays can be traced back to Conner and Jones in the early nineties.[55–58] Since then, the resolution of synchrotron-based X-ray techniques has steadily improved, advancing from microns to nanometers. For example, 2D STXM has been used to image and correlate the speciation of polyethylene, chromium (Cr) and titanium (Ti) in microtomed cross-sections of Cr- and Cr/Ti-based Phillips catalysts at 50–100 nm spatial resolutions (ex situ; recorded at STXM end stations at the Canadian Light Source (CLS), Advanced Light Source (ALS) and Swiss Light Source (SLS), Figure 4).[59,60] The technique has also recently been employed to study the orientation of polymer chains in low- and high-density regions of stretched polyethylene.[61]

In the field of 3D imaging, high spatial resolutions have been achieved with ptychographic X-ray computed tomography (PXCT), a phase contrast-based method that combines scanning X-ray microscopy with coherent diffraction

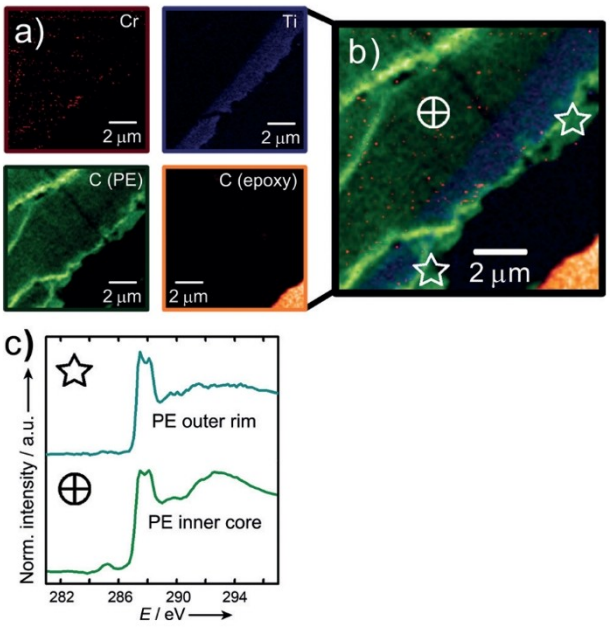

Figure 4. Elemental maps of a Phillips-type Cr/Ti/SiO_2 catalyst particle cross-section after ethylene pre-polymerization at 100 °C and 1 bar ethylene pressure (Cr: dark red, Ti: blue C, C from polyethylene: green, C from the epoxy resin: orange) as recorded with soft X-ray spectromicroscopy (scanning transmission X-ray microscopy, STXM). C K-edge X-ray absorption spectroscopy (XAS) revealed different types of polyethylene in the interior and at the edge of the microtomed catalyst particle. The measurements were performed at the beamline 10ID–1 at the Canadian Light Source (CLS). Reproduced from ref. [59]. Copyright © 2015 Cicmil et al., published by Wiley-VCH Verlag.

imaging.[62] Ptychography was combined with X-ray fluorescence (XRF) microscopy at the P06 beamline at PETRA III (Deutsches Elektronen-Synchrotron, DESY) to visualize the distribution of titanium-containing support fragments within an individual 40 µm Ziegler–Natta catalyst particle that was pre-polymerized with propylene (Figure 5).[37] A synergy between the sectioning and the layer-by-layer mechanism was reported. XRF microscopy yielded quantitative data on the distribution and concentration of Ti sites—an approach that is particularly advantageous when the phase contrast between the support and polymer is insufficient. In the future, XRF microscopy could potentially be applied to several other industrial polymerization catalyst systems, such as the Cr-based Phillips catalyst and Zr-based metallocenes, provided that the desired X-ray absorption edge falls within the energy range of a given imaging set-up and self-absorption effects remain limited.

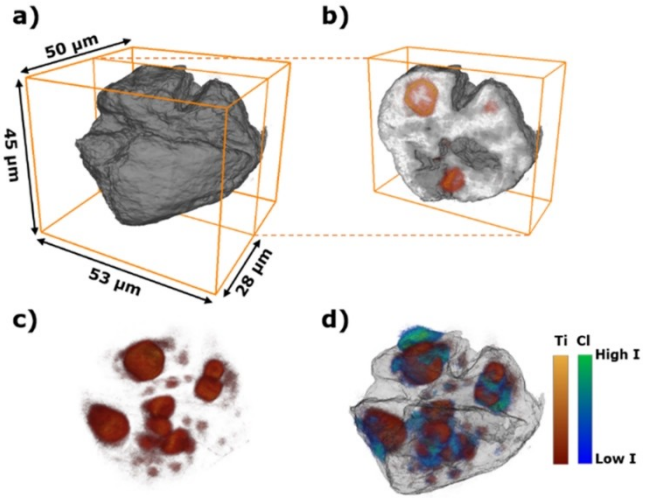

Figure 5. Reconstructed 3D volume of a propylene-polymerized Ziegler – Natta catalyst particle [electron density reconstruction: gray scale, Ti X-ray fluorescence (XRF) signal: red, Cl XRF signal: green]. The particle was characterized with hard X-ray ptychography and XRF at the P06 beamline, PETRA III, Deutsches Elektronen-Synchrotron (DESY). Reproduced from ref. [37] under the CC-BY-NC-ND license. Copyright © 2020 American Chemical Society.

The PXCT set-up at beamline P06 was also used to characterize an ensemble of 434 ethylene pre-polymerized Ziegler catalyst particles over a time period of 22 h (theoretical median diameter after polymerization: $D_{50,\ polymerized} = 5.9$ µm, 120×120×20 µm^3 field of view).[63] A 3D spatial resolution of 74 nm was determined via Fourier shell correlation (FSC) analysis. The large number of characterized particles facilitated a statistical evaluation of the degree of support fragmentation via image segmentation and processing algorithms (Figure 6). Similar to the above-mentioned studies on silica-supported olefin polymerization catalysts, the analysis revealed contributions from both the layer-by-layer and sectioning mechanism, with the latter more heavily involved in particles displaying advanced fragmentation degrees.

While ptychography clearly sets the benchmark in terms of spatial resolution, phase contrast-based full-field holotomography enables significantly higher sample throughput due to its shorter measurement times. Recent holotomography measurements at beamline ID16B at the European Synchrotron Radiation Facility (ESRF) of pre-polymerized metallocene-based catalyst particles, with diameters equal to or larger than 40 µm, only took 10–15 min per particle (Figure 7A). The samples were measured at four sample-to-detector distances. With the technique yielding clear contrast between low atomic number (Z) polyethylene and silica (Figures 7A and 7B), it represents a promising alternative to ptychography, especially when larger sample sets or particles are under investigation. The GINIX holotomography set-up at the P10 beamline at PETRA III (DESY) was also used to investigated a silica-supported metallocene ($D_{50,\ pristine} = 25.0$ µm) at multiple reaction stages.[31] A quantitative assessment of the particles' support and pore space architectures revealed large structural heterogeneity at five different reaction stages (Figure 7B). As structural parameters govern the degree of mass trans-

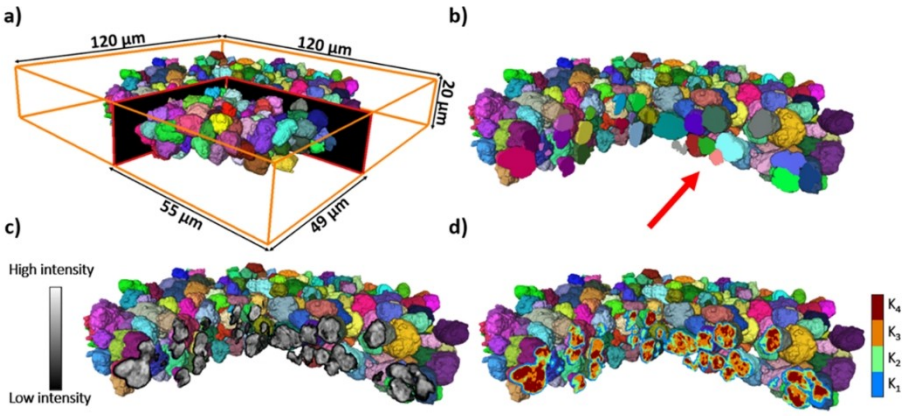

Figure 6. Reconstructed 3D volumes of 434 pre-polymerized Ziegler catalyst particles that were segmented with a k-means clustering algorithm to quantify their morphological heterogeneity. The particles were measured with hard X-ray ptychography at the P06 beamline, PETRA III, DESY. Reproduced from ref. [63] under the CC BY-NC-ND 4.0 license. Copyright © 2021 Bossers et al., published by American Chemical Society.

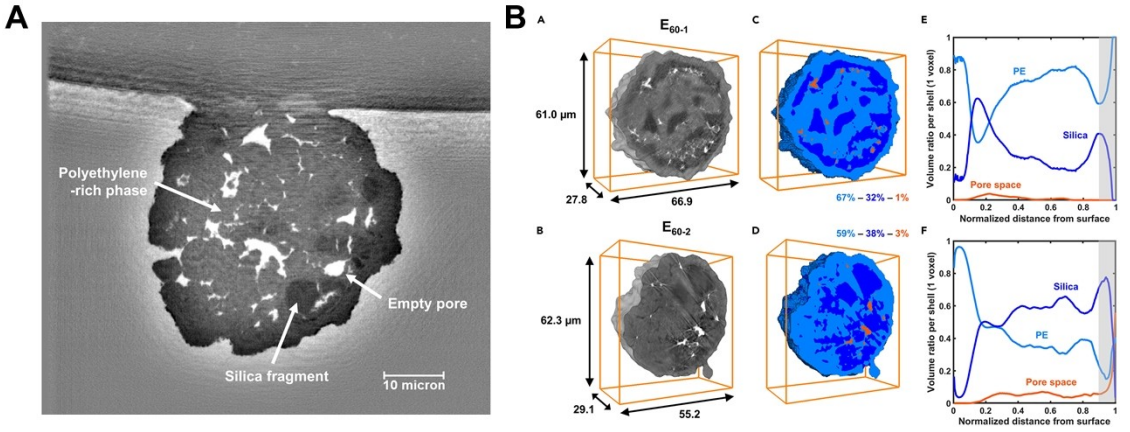

Figure 7. A: Reconstructed virtual cross-section of a zirconocene-based catalyst particle that was pre-polymerized in slurry-phase for 5 min at 10 bar ethylene and room temperature (unpublished data; light grey = polyethylene-rich phase, dark gray = silica-rich phase, white = macropore space). The particle was measured with hard X-ray holotomography at the ID16B beamline at the European Synchrotron Radiation Facility (ESRF) in less than 15 min. B: Reconstructed and segmented grayscale volumes of two hafnocene-based catalyst particles that were pre-polymerized in gas-phase for 60 min at 1.6 bar ethylene pressure and room temperature. The particles were measured with hard X-ray holotomography at the P10 beamline, PETRA III, DESY. Radial phase distribution analysis clearly demonstrated significant inter- and intraparticle heterogeneity amongst particles from the same batch. Reproduced and reprinted from ref. [31], Copyright © 2021, with permission from Elsevier Inc.

port through the particles, they have a significant influence on the particles' morphological evolution upon polymerization.

Last but not least, laboratory-based computed tomography (CT), an absorption contrast-based technique, represents an accessible alternative to synchrotron-based methods for characterizing pristine and polymerized catalyst particles.[28,48,64–66] Nano-computed tomography (nanoCT) has been reported to deliver sub-180 nm resolutions for different silica-supported olefin polymerization catalysts (Figure 8), as determined via Fourier shell correlation analysis (FSC).[48] In general, laboratory-based CT instruments offer experimental and operational flexibility to researchers who do not have regular access to synchrotron facilities.

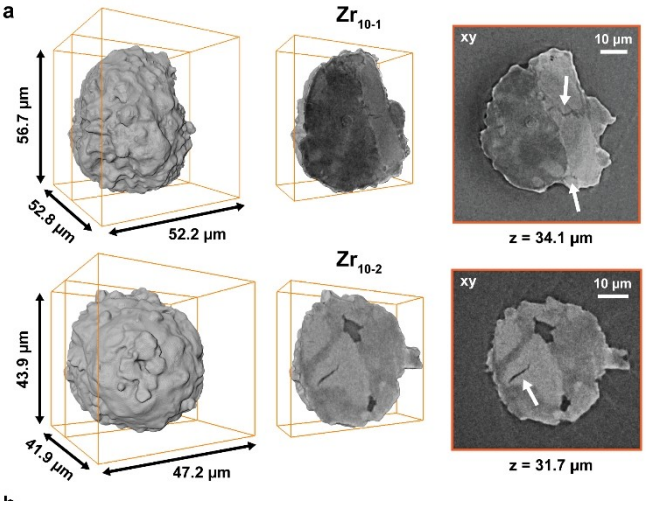

Figure 8. Reconstructed particles and virtual cross-sections of two zirconocene-based catalyst particles that were pre-polymerized in slurry-phase for 1 min at 10 bar ethylene pressure and room temperature (light grey = silica-rich phase, dark gray = polyethylene-rich phase, dark gray/black = macropore space). The data was acquired with laboratory-based nano computed tomography (nanoCT) to study the propagation of extensive cracks in the support (indicated by white arrows) was studied. Reproduced and adapted from ref. [48] under the CC BY 4.0 license. The figure is an excerpt of the original. Copyright © 2022 Werny et al., published by Wiley-VCH.

2.3. Optical microscopy

Optical microscopy has been widely applied in the field of synthetic polymers[67] and olefin polymerization, delivering information on the composition, formation and morphology of polymers, as well as on kinetics of polymerization reactions. For instance, Blum et al. have used fluorophore-tagged olefin monomers and microscopy to visualize ring-opening metathesis polymerization (ROMP) reactions in situ.[68–70] The group was able to identify a preferential formation of fluorescent polymer on a homogeneous Grubbs catalyst in solution rather than on a heterogeneous Grubbs catalyst (Figure 9A).[68] Chen et al. studied the ROMP of norbornene, also catalyzed by a Grubbs catalyst, using optical microscopy.[71,72] By monitoring the height of a tethered magnetic particle, they were able to measure the extension of the growing polymer chain under reaction conditions (Figure 9B). Interestingly, the extension of the polymer chain was not continuous and linear due to conformational entanglements arising from newly incorporated monomers.

In the field of industrially applied olefin polymerization catalyst systems, various groups have used optical video microscopy, together with appropriate reaction cells, to track the growth of individual catalyst particles during gas-

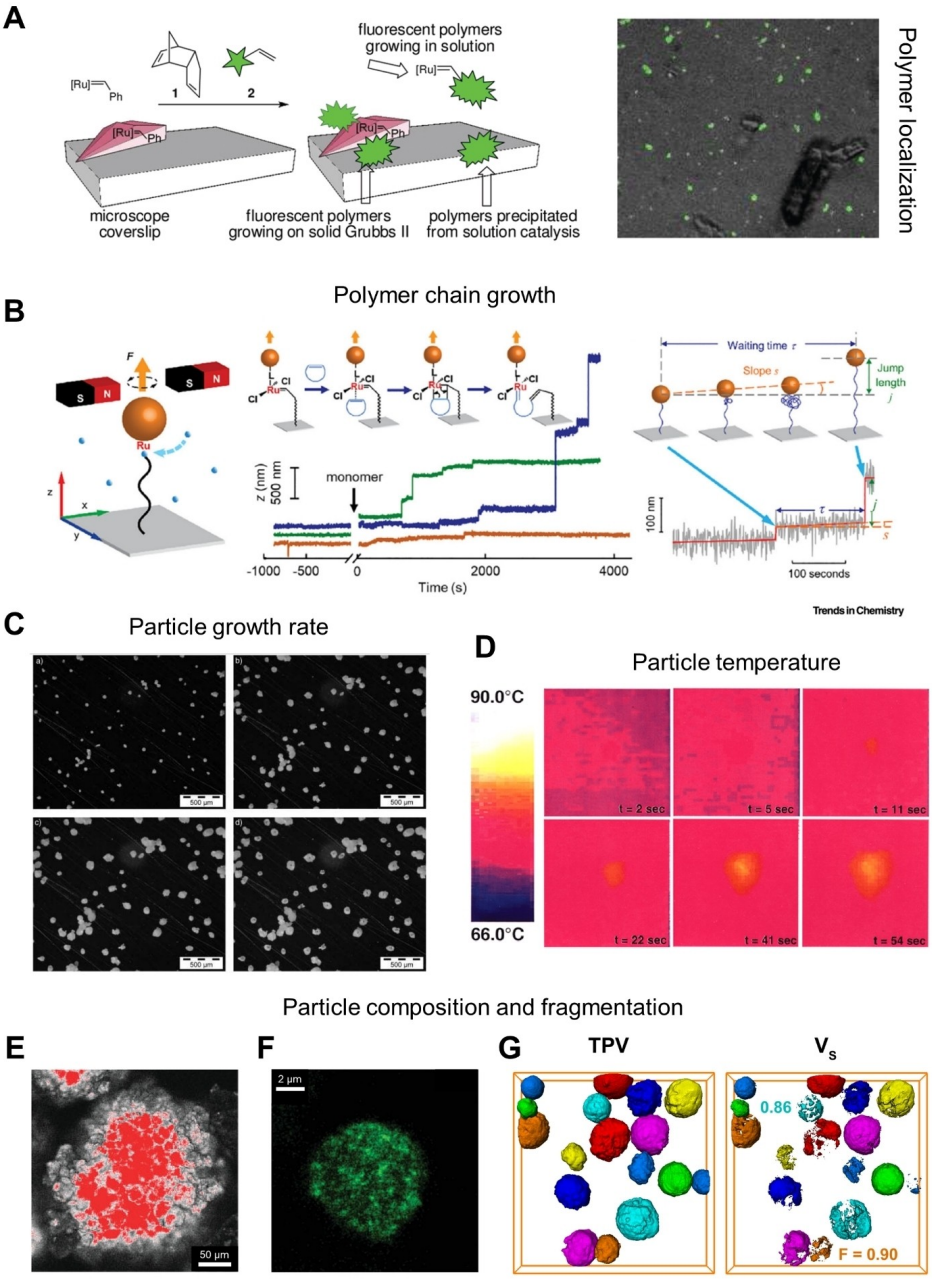

Figure 9. Chemical information that can be extracted from supported olefin polymerization catalysts with optical microscopy. A: Ruthenium-catalyzed polymerization of a fluorophore-tagged olefinic monomer. The resulting fluorescent polymer was localized with fluorescence microscopy. Reproduced and adapted from ref. [68]. The figure is an excerpt of the original. Copyright © 2011, American Chemical Society. B: Real-time extension-versus-time trajectory for a growing polymer chain during a Grubbs catalyst-mediated ring opening metathesis polymerization. Reproduced and adapted from ref. [72]. The figure is an excerpt of the original. Copyright © 2021 Elsevier Inc. All rights reserved. C: Optical images recorded of silica-supported metallocene catalyst particles during gas-phase ethylene polymerization at 10 bar ethylene pressure and 60 °C (reaction stages: 0 min, 60 min, 120 min, and 180 min) that were used to assess their respective growth rates. Reproduced from ref. [77]. Copyright © 2003 Wiley-VCH; published by John Wiley and Sons. D: Infrared images recorded of a Ziegler–Natta catalyst particle during olefin polymerization, yielding insights into the temperature of the particle. Reproduced from ref. [80]. Copyright © 2003 American Institute of Chemical Engineers (AIChE), published by John Wiley and Sons. E: Confocal fluorescence microscopy (CFM) image of an ethylene polymerized metallocene/MAO/X-based catalyst (MAO = methylaluminoxane and X = perylene-stained silica support), revealing its internal morphology. Reproduced and adapted from ref. [83]. The figure is an excerpt of the original. Copyright © 2005 Wiley-VCH Verlag, published by John Wiley and Sons. F: CFM image of an ethylene polymerized metallocene/MAO/Y-based catalyst, with Y = porous, rhodamine B-stained polyurethane support. Reproduced and adapted from ref. [85]. The figure is an excerpt of the original. Copyright © 2013 Wiley Periodicals, Inc.; published by John Wiley and Sons. G: Reconstructed 3D CFM data of multiple autofluorescent zirconocene/MAO/SiO_2 particles after ethylene pre-polymerization (with TPV = total particle volume; V_S = Volume of silica-dominant domains; fragmentation parameter $F = (1\text{-}V_S)/TPV$). The figure is an excerpt of the original. Reproduced and reprinted from ref. [87] under the CC BY 4.0 license. Copyright © 2022 Werny et al., published by American Chemical Society. In E–G, the support has been impregnated with a fluorophore, while the formed polymer is not fluorescent.

phase polymerization reactions (Figure 9C).[73–79] Pater et al. even studied the temperature evolutions of individual catalyst particles under reaction conditions using infrared imaging (Figure 9D).[80] A more widely applicable approach was introduced by the group of Mülhaupt, who used video microscopy and focused beam reflectance measurement (FBRM) probes to monitor the growth of catalyst particles during slurry-phase polymerizations in a stirred reactor.[81] In contrast to many of these efforts, which delivered information on particle growth and kinetics, the Müllen group employed laboratory-based confocal fluorescence microscopy (CFM), in combination with specific support staining procedures, to determine the internal morphology and composition of supported olefin polymerization catalysts (Figures 9E and 9F).[82–85] In these studies, the distribution of the support in the polymer matrix was assessed non-invasively based on its fluorescence, thus yielding insights into the process of fragmentation. Müllen et al. also introduced the use of perylene-based dyes to differentiate between several silica-supported metallocenes, employed in the same polymerization run, using UV light.[86] Certain silica-supported metallocenes are even known to exhibit autofluorescence and are thus suitable for a direct characterization via CFM. Our group recently combined CFM with advanced image processing to quantitatively assess support fragmentation in a large number of autofluorescent metallocene-based catalyst particles.[87] This delivered representative insights into inter- and intraparticle heterogeneity during the early stages of ethylene polymerization at 10 bar ethylene pressure (Figures 9G).

2.4. Other techniques

Scanning probe techniques such as atomic force microscopy (AFM),[88–90] atomic force microscope-infrared spectroscopy (AFM-IR),[91–93] and infrared photoinduced force microscopy (IR PiFM)[38,94–96] represent powerful tools to assess the topology and morphology of polymer materials at high spatial resolutions down to a few nanometers. In a study by Ruddick et al., phase-imaging AFM was used to study the fragmentation of a Phillips catalyst at different stages of ethylene polymerization.[97] Larger support fragments were detected at the surface of the polymerized catalyst. The authors postulated that these larger fragments, owing to their smaller surface areas, were less active in comparison to smaller fragments and thus pushed to the surface of the catalyst during polymerization. In a more recent study, IR PiFM was used to image cross-sections of an ethylene pre-polymerized hafnocene catalyst particle at sub-20 nm resolution.[38] IR maps were recorded at characteristic wavenumbers for the Si–O stretching vibration of silica (SiO_2) and the symmetric C–H bending vibration of the methylene (CH_2) group (Figure 2B). A clear spectroscopic differentiation between the silica support and formed polyethylene was thus obtained, thereby helping to identify fragmentation pathways and visualize crack formation. The two phases were also clearly distinguishable in the phase imaging mode, which is suitable for assessing mechanical material properties. Further studies could employ quantitative nanomechanical mapping (QNM) and nano indentation testing to quantify mechanical material properties, such as elasticity, via the Young's modulus.[98] Besides the above-mentioned techniques, Raman microscopy can also be used to monitor the formation and distribution of polymer.[46] hile the technique's resolution is lower, it has the benefit of being able to capture larger sample areas in comparatively short measurement times.

3. Determining the distribution of polymer and related decomposition products in polyolefin cracking catalysts

During catalytic pyrolysis, hydrocracking and hydrogenolysis, polyolefins, such as PP and PE, are converted to a mixture of aliphatic, aromatic and olefinic hydrocarbons. As the reaction is conducted at elevated temperatures, the polymers melt to form viscous fluids that may infiltrate the pore space of catalyst particles. Thermal pre-cracking of the polymer chains to shorter chains is hypothesized to occur, which increases the accessibility of shorter chains and intermediate cracking products to the particle interior for further reactions.[11] A similar effect may be achieved with other (thermo−)chemical (e.g., non-catalytic pyrolysis, solvolysis, dissolution/precipitation, etc.[8]) and mechanochemical methods (e.g., ball milling[99–101]) that reduce the average polymer chain length. In general, as the polymer decomposition reaction proceeds, a more extensive dissociation of the polymer chains takes place. Furthermore, subsequent aromatization of the formed intermediates results in the formation of different coke species. Both the degree of polymer intrusion into the pores of a given catalyst body and the distribution of coke species can be visualized with different high-resolution imaging techniques.

3.1. Electron microscopy

Focused ion beam-scanning electron microscopy (FIB-SEM) represents an accessible characterization tool to obtain data on polymer localization and mobility. The technique is suitable for assessing the degree of polymer intrusion and pore utilization in macroporous catalyst particles that have been contacted with polyolefins at elevated temperatures. This can yield insights into the roles of a polymer's viscosity and a catalyst's pore space accessibility on the performance of a given catalyst. Further studies could utilize a combinatorial SEM-EDX-CFM (EDX = energy dispersive X-ray spectroscopy, CFM = confocal fluorescence microscopy) approach to determine the chemical composition of different phases with distinct reactivities (e.g., coking or specific interactions with probe molecules) in a catalyst particle cross-section, thereby helping to identify structure-performance relationships.

3.2. X-ray microscopy

X-ray microscopy can provide information on the degree of polymer intrusion into the pores of a given catalyst particle in 3D. Recent hard X-ray holotomography measurements on FCC and equilibrium FCC catalyst (ECAT) particles, used for a limited amount of time in the catalytic pyrolysis of low molecular weight PP, revealed differences in the degree of polymer intrusion (Figure 10A). These are mostly likely associated with the particle architecture and the degree of porosity in the outer layers of the catalyst particles. In fact, the studied ECAT particles, in contrast to most of the FCC particles, were found to possess an internal pore structure that was more accessible for PP. Furthermore, coke deposits were clearly detectable in the particles (Figure 10A). This stands in agreement with previous experiments by Vesely et al., who first demonstrated the suitability of holotomography for detecting and quantifying

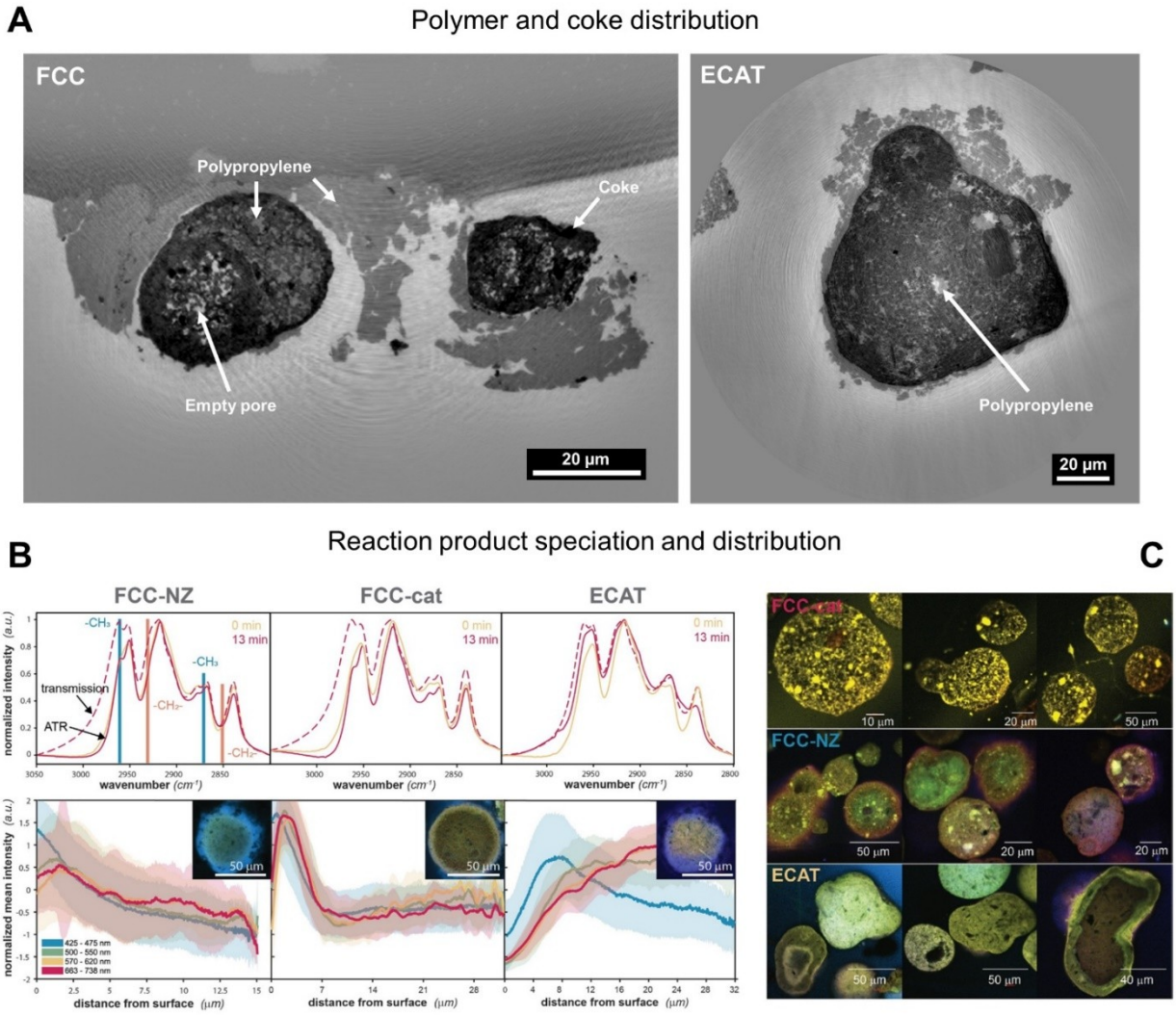

Figure 10. Information obtained on polyolefin cracking catalysts via high resolution X-ray and optical microscopy. A: Reconstructed virtual cross-sections of fluid catalytic cracking (FCC) and equilibrium cracking catalyst (ECAT) particles that have partially reacted with polypropylene (PP) at 250 °C (details about the samples and reaction conditions can be found in ref. [11]). Differences in the degree of polymer intrusion between the particles as well as high local concentrations of coke (high electron density, dark grey) are clearly visible. The particles were measured with holotomography at beamline ID16B at the European Synchrotron Radiation Facility (ESRF, unpublished data). B: Confocal fluorescence microscopy (CFM) images and Fourier-transform infrared spectroscopy (FTIR) spectra of PP/catalyst mixtures after quenching the reaction at 250 °C. Radial intensity profiles, based on the measured CFM images, indicate differences in the distribution of fluorescent reaction products between FCC/FCC-NZ and ECAT (FCC-NZ=FCC catalyst, No Zeolite; and ECAT = equilibrium cracking catalyst). All samples were microtomed prior to characterization with CFM. Reproduced from ref. [11] under the CC BY 4.0 license. Copyright © 2021 Vollmer et al., published by Wiley-VCH. C: CFM images recorded of FCC, FCC-NZ and ECAT catalysts after a full reaction run with PP at ≈450 °C. All samples were microtomed prior to characterization with CFM. High concentrations of fluorescent aromatics and coke species are visible as distinct yellow domains. Reproduced from ref. [11] under the CC BY 4.0 license. The figure is an excerpt of the original. Copyright © 2021 Vollmer et al., published by Wiley-VCH.

coke in FCC catalyst particles.[102] In the future, both the distribution and volume of coke can be quantified by scanning reacted polyolefin cracking catalyst particles before and after calcination (i.e., via differential contrast tomography, as reported by Vesely et al.[102]). The tomographies can then be used to simulate the diffusion of reaction intermediates and products through the macropore space of the catalyst particle, both in the presence and absence of polymer, as well as coke. Experiments by Weber et al. on Ni/Al_2O_3 catalysts demonstrated that coke deposits can also be localized with hard X-ray ptychography (PXCT) at high spatial resolutions (sub-100 nm).[103] With the resolution of imaging set-ups steadily improving, it may soon be possible to image the process of pore filling in the mesopore regime (i.e., 2–50 nm). The spatial distribution of certain catalyst components, in relation to, for example, formed coke species, could also be probed with transmission X-ray microscopy (TXM), X-ray fluorescence tomography (XRF) and X-ray diffraction (XRD) tomography.[102,104–108]

3.3. Optical microscopy

While electron and X-ray microscopy provide unparalleled spatial resolutions in 2D and 3D, confocal fluorescence microscopy (CFM) can provide complementary information on the formation and distribution of fluorescent reaction products, such as aromatics and coke, in multiple catalyst particles. Vollmer et al. used CFM to study the formation and localization of early-stage cracking products in fluid catalytic cracking particles (i.e., FCC/FCC-NZ, with NZ=No Zeolite), and equilibrium FCC catalyst (ECAT) particles, after a 13 min reaction with polypropylene (PP) at 250 °C (Figure 10B, bottom).[11] In general, higher fluorescence intensities were observed in the outer rings of FCC and FCC-NZ catalyst particles, indicating that cracking and possibly aromatization were predominantly occurring at the particle surface and sub-surface regions. In the case of ECAT, on the other hand, the radial fluorescence intensity profile increased towards the center of the particles. This was linked to the presence of metal deposits (i.e., Fe, Ni, and V), which are expected to increase the pre-cracking activity of the catalyst matrix, thereby enhancing the transport of cracking products and reaction intermediates into the particle interiors, where they subsequently form aromatics. Attenuated total reflectance-infrared spectroscopy (ATR-IR) and transmission Fourier-transform infrared (FTIR) spectroscopy helped to further assess the degree of cracking in the bulk PP surrounding the catalyst particles and in the catalyst/PP composite, respectively (Figure 10B, top). While cracking products were only detected in higher concentrations inside or in close vicinity of the FCC and FCC-NZ catalyst phase, cracking products were also observed in the bulk PP surrounding the ECAT catalyst particles. The authors attributed this to reaction products that had diffused out through the plastic layer surrounding the ECAT catalyst material.

CFM measurements were also performed on all catalysts after a full reaction run with PP at ≈450 °C. Well-defined bright spots, observed in FCC catalyst particles and allocated to high local aromatics and coke concentrations in zeolite domains, were not visible in the ECAT catalyst (Figure 10C). The authors postulated that the zeolite domains are less accessible in ECAT due to metal deposits. The domains may have also been deactivated via streaming in the regenerator of the FCC unit. Despite this, all catalysts formed significant amounts of aromatics, suggesting that zeolite is not necessary for the aromatization of PP. The bright features in FCC only appeared after a full reaction run, which further confirmed the hypothesis that pre-cracking in the catalyst matrix precedes aromatization in the zeolite domains.

Future research efforts may be directed towards the rational design of highly porous catalysts that are potentially more suitable for the conversion of viscous polymers. By using CFM, particle accessibilities and activities can easily be determined for catalysts with different porosities and pore space architectures, based on the fluorescent coke species that are formed. Furthermore, pristine catalyst particles can be stained with fluorophores and (reactive) probe molecules to visualize their 3D structure, activity, as well as the distribution of different components and catalytically active phases.[109–111] Fluorophore-tagged polymers could even be used to study polymer melting and intrusion into the pores of a given catalyst with CFM.

4. In situ and operando characterization of individual catalyst particles for olefin polymerization and polyolefin decomposition

In situ and operando (Figure 11A) X-ray microscopy at the nanometer length scale represents a powerful approach for obtaining more detailed insights into the behavior of heterogeneous catalysts under operating conditions.[53,54,112,113] Generally speaking, this requires the implementation of sophisticated micro- and nanoreactor systems with low dead volumes, suitable windows or capillaries for high X-ray transmission (e.g., Si_3N_4 or quartz), as well as stable gas flows under high-temperature and high-pressure operating conditions.

In 2008, our group started using reactor set-ups with integrated MEMS (microelectromechanical systems) chips for performing 2D scanning transmission X-ray microscopy (STXM) on different types of Fischer–Tropsch catalysts (Figure 11B) under in situ and operando conditions (up to 4 bar and 500 °C).[114–116] In general, the use of soft X-rays often requires the use of relatively thin samples (≤1 μm) in comparison to hard X-ray-based tomography experiments. More recently, Grunwaldt et al. reported on another reactor design featuring a MEMS chip for complementary X-ray nano-imaging and spectroscopy under reaction conditions (Figure 11C). Using this reactor, 3D X-ray ptychographic measurements can be performed at 1 bar pressure and at temperatures of up to 1100 °C, covering an angular range of ±35 °.[117]

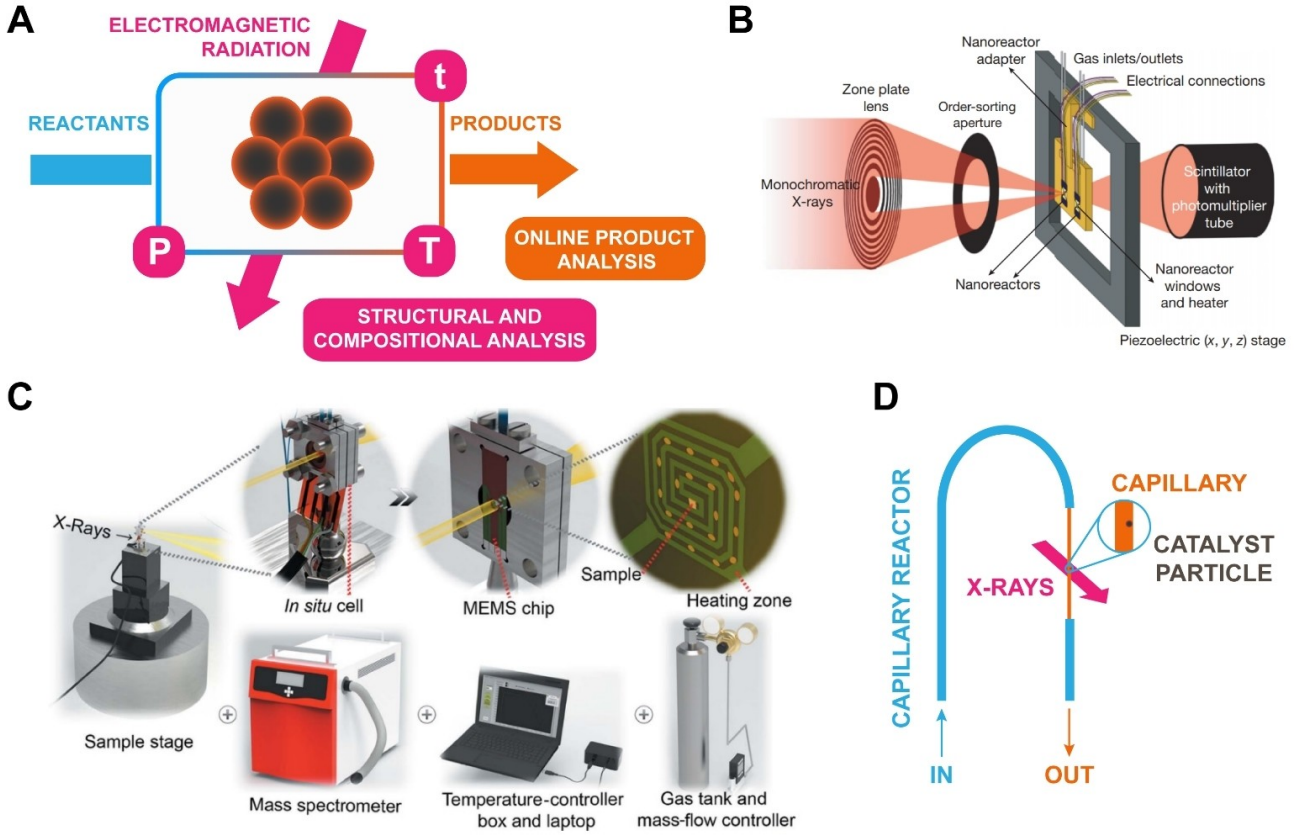

Figure 11. A: Schematic of the operando spectroscopy approach for characterizing catalysts in their working state. The structure and chemical composition of the catalyst is monitored directly under reaction conditions, while simultaneously assessing the formed reaction products (e.g., via gas chromatography or mass spectrometry). B: Scanning transmission X-ray microscopy (STXM) set-up first used by Weckhuysen, de Groot et al. to study Fischer–Tropsch synthesis catalysts in situ. The measurements were performed at beamline 11.0.2 of the Advanced Light Source (ALS) at the Lawrence Berkeley National Laboratory, USA. Reproduced and adapted from ref. [115]. Copyright © 2008, Macmillan Publishers Limited. All rights reserved. C: Schematic of the reactor set-up used by Grunwaldt et al. for in situ 2D and 3D ptychography at the P06 nanoprobe beamline of PETRA III, Deutsches Elektronen-Synchrotron (DESY). Reproduced from ref. [117] under the CC BY 4.0 license. Copyright © 2019 Fam et al., published by International Union of Crystallography. D: Simplified illustration of the capillary-based microreactor employed by Weckhuysen et al. for in situ transmission X-ray microscopy (TXM) experiments at Beamline 6–2c of the Stanford Synchrotron Radiation Lightsource (SSRL).

Capillary-based microreactors[118,119] represent a promising alternative to reactors with integrated MEMS devices as they enable significantly higher angular ranges. The technical challenge here, however, remains in using heating equipment that is compatible with the sensitive beamline optics, both in terms of the released heat and spatial constraints. In 2012, our group started using capillary-based microreactor systems (capillary diameter = 100 µm) with appropriate heating devices for in situ transmission X-ray microscopy (TXM) on catalyst particles at 1–30 bar and up to 600 °C.[120–123] In a more recent design, the quartz or Kapton capillary is attached to a holder (Figure 11D, simplified schematic) with heat-resistant epoxy while the heating is provided by a nichrome wire in a cylindrical chamber. A water-cooled aluminum cage with X-ray windows prevents overheating of the optical components.

Over the last years, capillary-based reactor systems have become increasingly established and have been used to study different heterogeneous catalysts with various X-ray-based imaging techniques at length scales ranging from millimeters to nanometers.[124–128] Future efforts must, however, be directed towards designing compact reactor systems (e.g., chip-based reactors as reported by Drake et al.[129]) that have integrated heating and cooling elements, while also enabling high gas pressures and, hence, realistic reaction conditions. Reactors with low spatial requirements are advantageous as they will ensure a given reactor's compatibility with multiple imaging set-ups and beamlines. Furthermore, the number of missing imaging angles should be minimized in future reactor designs (see design by Holler et al.[130]) to limit reconstruction artefacts and guarantee the highest possible imaging resolution.

In the context of olefin polymerization catalysts, sophisticated reactors will provide the means for tracking the morphological evolution of individual catalyst particles in situ. The main challenge remains in maintaining the stability of the air- and moisture-sensitive catalyst particles that are loaded into the reactor inside an inert environment (e.g., glovebox). Due to the relatively fast polymerization rates, a pulsing approach with ethylene and an inert gas may have to

be adopted. The previously mentioned holotomography set-up at ID16B (ESRF, Figure 7A) enables high temporal and spatial resolutions and would therefore be suitable for such *quasi* in situ measurements.[131–133] With the flux and coherence of synchrotron radiation as well as the speed of microscopy set-ups and detectors steadily improving,[134–136] it may even become possible to monitor polymerization reactions live (i.e., true in situ/operando experiments without pulsing) at spatial resolutions of a few tens of nanometers. To maximize the temporal resolution, however, it could be beneficial to perform measurements at slightly lower spatial resolutions. The acquired data would provide valuable input for refining existing models that are used to simulate support fragmentation.[27,28,137]

Catalysts for polymer decomposition, on the other hand, can be loaded with a limited amount of polymer and subsequently imaged with X-ray nanotomography. Ideally, tomographies are collected before, during, and after the reaction, while monitoring both the reactants and the reaction products. This could provide insights into (i) the intrusion of polymer into the particle, (ii) polymer decomposition, and (iii) coke formation.[102]

By using suitable reaction cells (e.g., cells by Linkam Scientific, Harrick Scientific Products Inc.), confocal fluorescence microscopy (CFM) can also potentially be used to study heterogeneous polymerization and (hydro)cracking catalysts under working conditions. Provided the concentration of fluorophore is sufficiently high, structural and chemical changes to catalysts may be observed in real time. The decomposition of polymers on polymer decomposition catalysts may be imaged in situ or operando due to the high concentration of fluorescent coke species that are formed. Thus, by correlating changes in the fluorescence of the formed intermediates and products and the monitored composition of gas-phase products, new structure–activity correlations may be obtained.

5. High-throughput experimentation and machine learning to assess interparticle heterogeneity in olefin polymerization and polyolefin decomposition catalysts

Industrially applied catalysts, such as supported olefin polymerization catalysts[29,31] and cracking catalyst (e.g., FCC/ECAT),[30] are per definition heterogeneous in nature. The degree of heterogeneity and any associated chemical implications thereof are, however, poorly understood. Optical and X-ray (fluorescence) microscopy techniques can bridge the gap between single catalyst particle studies and bulk catalyst characterization approaches and help to elucidate relevant structure-performance relationships in a statistically relevant number of catalyst particles.

In the field of heterogeneous olefin polymerization catalysts, confocal fluorescence microscopy (CFM), in synergy with automated image segmentation (e.g., via machine learning) and data analysis, has the potential to become a high-throughput tool for determining the morphology of multiple catalyst particles after synthesis as well as after (pre)-polymerization (quality control). While the acquisition of 2D data provides a mean of comparing and screening different reaction stages and catalyst batches at high sample throughput (in the range of 10^2–10^3 particles per h), 3D imaging can be used to accurately assess the composition of multiple catalyst particle sub-volumes in a limited space of time (~ 2 h scan time for a 178 μm×178 μm×30 μm field of view[87] Material-specific staining procedures,[82,83,85] autofluorescent catalysts, fluorophore-tagged monomers[69] and fluorescent probe molecules (e.g., fluorescent external/internal donors for Ziegler–Natta catalysts) will help to extend the methodology to a variety of supported olefin polymerization catalysts. In the field of X-ray microscopy, hard X-ray holotomography and ptychographic X-ray computed tomography are particularly well suited to measuring large sample sets of polymerization catalyst particles in 3D.[31,63] Automated image reconstruction, segmentation[138–141] and analysis can greatly improve the efficiency of the data analysis. This, in turn, will further increase the throughput of the techniques and will help to deliver statistically relevant chemical insights. Next-generation synchrotrons and instrumental advances will most likely make X-ray microscopy the method of choice for collecting high-resolved morphological data on a representative number of particles 3D. Finally, planar model olefin polymerization catalyst systems,[142–148] potentially in form of spherical caps or micro-islands[46] (Figure 12A), could find application in high-throughput catalyst characterization and testing studies. By targeting a large number of islands with various micro-spectroscopic tools, correlations between the composition and structure of the employed catalyst material and the morphology, composition and crystallinity of the formed polymers can be investigated. Furthermore, islands of different chemical compositions could be screened in parallel under identical reaction conditions. This could also be realized with small wafers, featuring different catalyst and co-catalyst formulations, that are placed in the same reaction cell or chamber. By installing the required analytical instruments inside for example, a glovebox, samples could even be characterized at multiple reaction stages.

In the field of cracking catalysts, high-throughput approaches have already been implemented. Kerssens et al. were able to optically differentiate between FCC particles containing either zeolite Y or ZSM-5 in a mixed catalyst batch of 25000 catalyst particles after a chemical staining reaction with 4-fluorostyrene.[110] Furthermore, by using 4-methoxystyrene as a fluorescent probe molecule, they were able to assess the acidity (considered as representative for the catalytic activity) and micropore volume of the catalyst particles (Figure 12B). A similar approach could be applied to FCC catalysts after different stages of polyolefin decomposition to study their accessibilities and acidity as a function of time. Nieuwelink et al. have studied interparticle heterogeneities in density-separated fractions of a ECAT catalyst by overlaying Fe and Ni X-ray fluorescence (XRF) maps with CFM images recorded after reaction with different probe molecules.[30] The degree of deactivation was linked to the Ni content of a given particle. Both studies

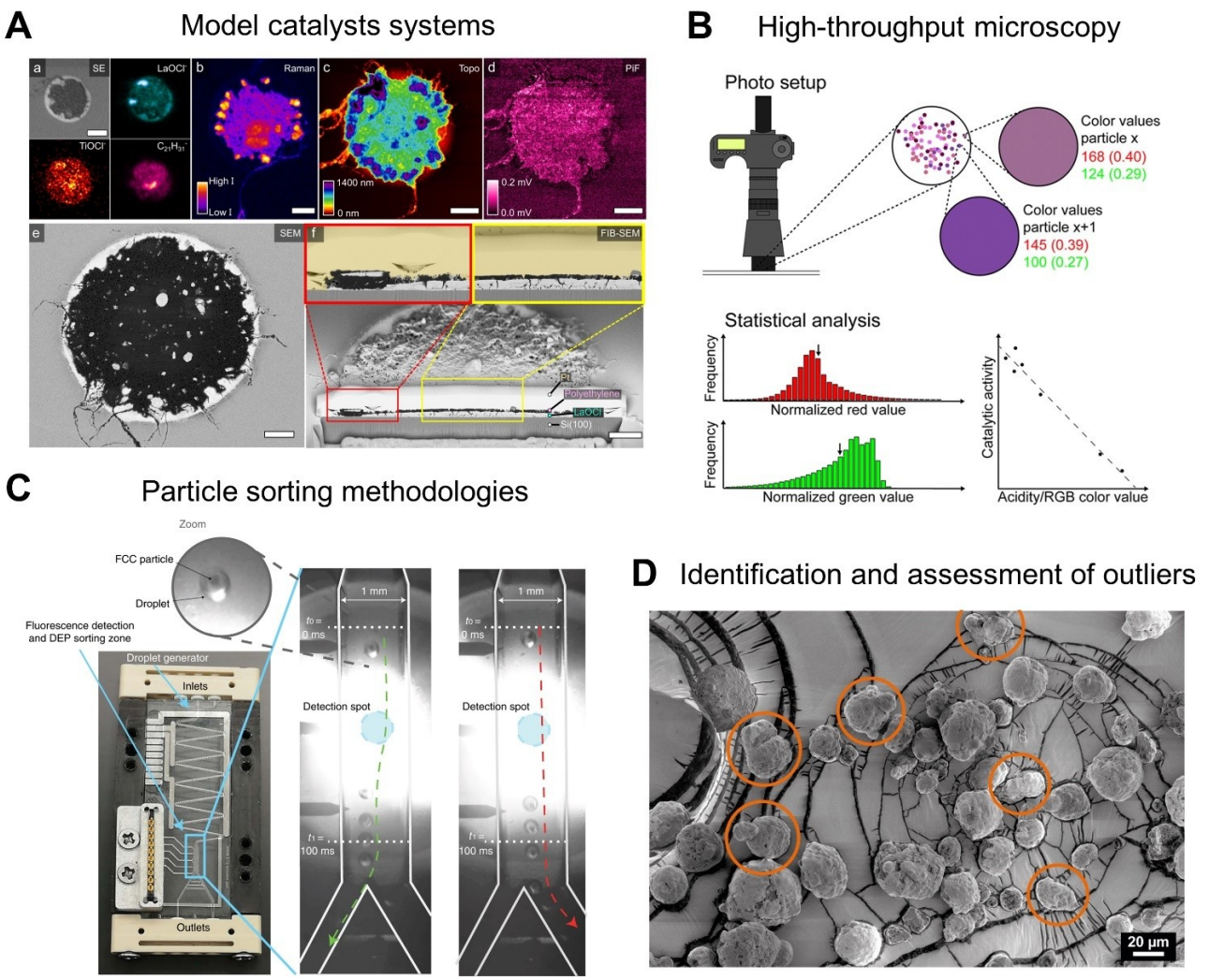

Figure 12. Synthetic and analytical approaches that can be exploited to obtain representative insights into the chemical behavior of heterogeneous catalyst materials, either at the level of one particle or multiple particles. A: Development of model catalyst systems that enable high-throughput characterization with 2D (spectro−)microscopy techniques. Reproduced from ref. [46] under the CC BY 4.0 license. Copyright © 2022 Bossers et al., published by Springer Nature. B: Implementation of high-throughput microscopy techniques and automated data analysis to characterize large sample sets. Reproduced from ref. [110] with permission from the Royal Society of Chemistry under the CC BY 3.0 license. C: Sorting approaches to divide single catalyst particles according to their composition, structure and reactivity. Reproduced and adapted from ref. [111]. Copyright © 2021, Nieuwelink et al., under exclusive license to Springer Nature Limited. D: Systematic studies to identify and assess individual catalyst particles with irregular morphologies (i.e., agglomerates formed during spray drying of the catalyst support; strongly elongated or irregularly shaped particles) or compositions under reaction conditions (unpublished SEM data).

could be implemented in a similar fashion for catalysts employed in polyolefin decomposition to study properties such as accessibility and acidity at the level of individual particles.

While certain structure–activity relationships have been established, the precise influence of particles with irregular structures and deviating chemical compositions is not well understood. Dielectrophoretic (Figure 12C) and magnetophoretic particle sorting approaches,[111,149] in interplay with suitable optical microscopy (e.g. fluorescence microscopy) and machine learning algorithms, could be used to separate catalysts according to different criteria. For instance, olefin polymerization catalyst and fluid catalytic cracking particles could be sorted according to their initial morphology, chemical composition (e.g., metallocene and co-catalyst loading in the case of olefin polymerization catalysts, metal contaminants in the case of ECAT) or activity (e.g., acidity based on reactions with probe molecules in the case of FCC/ECAT[110]). This would ultimately yield more uniform catalyst batches with narrower spreads in activity. Investigating the reactivity and morphology of outliers (Figure 12D) could potentially advance our understanding of their exact role in catalytic reactions. As a consequence, new insights into the structural, compositional, and chemical requirements for catalytic reactions will be gained.

6. Summary and Outlook

Synchrotron- and laboratory-based chemical imaging techniques have emerged as useful analytical tools for assessing the evolution of supported olefin polymerization catalysts in 2D and 3D. Electron, fluorescence and X-ray microscopy in particular provide representative chemical and morphological information at the nanoscale. The growing analytical toolbox, as discussed in this review, can be employed in a similar fashion to obtain new physicochemical insights into the process of polyolefin decomposition or cracking. By visualizing the decomposition and mobility of commodity polymers, such polypropylene and polyethylene, in individual catalyst particles, an improved mechanistic understanding for the underlying processes of catalytic pyrolysis, hydrocracking and hydrogenolysis can be obtained. Despite in situ and operando microscopy and tomography studies still being in their infancy within this field of research, they hold great promise for assessing structure-composition-performance relationships in single catalyst particles. Furthermore, spatial insights into catalyst activity may be obtained by employing luminescent nanocrystals that function as local temperature sensors,[150,151] while the local pressure build-up during polymerization could be tracked with the help of novel pressure sensors.[152] Temperature maps[153] and potentially pressure maps can thus be acquired under reaction conditions by using conventional microscope systems with suitable excitation sources. In the field of X-ray microscopy, multibeam X-ray ptychography, once fully developed, will significantly increase the available field of view and reduce scanning times, opening up new avenues for the characterization of polymerization and depolymerization catalysts at high sample throughput and unparalleled spatial resolutions.[154–156]

In general, technological advancements will gradually improve the sensitivity and speed of many of the here discussed characterization methods. This will allow for polymerization and cracking catalysts to be studied in greater detail, possibly under reaction conditions. Recently, Rejman et al. used in situ optical microscopy, in combination with ex situ electron microscopy, to assess transport limitations in fluid catalytic cracking catalysts and distinguish catalytic pyrolysis from the thermal pyrolysis of polypropylene.[157] The acquired insights will guide the design of improved catalyst systems, which will play an important role in making our society more sustainable and circular.

Acknowledgements

The research was funded by a grant from the Dutch Polymer Institute (DPI, P.O. Box 902, 5600 AX Eindhoven, The Netherlands) and represents a part of the Research Program of DPI project no. 813. F.M. (Utrecht University, UU) acknowledges additional funding from a Netherlands Organization for Scientific Research (NWO) VIDI grant (723.015.007). We further acknowledge the European Synchrotron Radiation Facility (ESRF) for provision of the synchrotron radiation facilities, more specifically beamline ID16B, to measure the data shown in Figure 10A. Julie Villanova (ESRF), Victor Vanpeene (ESRF), Luca Carnevale (University of Twente), Rafael Mayorga-González (UU) and Caroline Versluis (UU) are acknowledged for their experimental support at beamline ID16B (ESRF). Ina Vollmer (UU) and Michael Jenks (UU) are thanked for providing the FCC and ECAT particles for the holotomography measurements at ID16B. Thomas Hartman (UU) is acknowledged for the cover image.

Conflict of Interest

The authors declare no conflict of interest.

Data Availability Statement

The data that support the findings of this study are available from the corresponding author upon reasonable request.

Keywords: Catalysis · Catalyst Fragmentation · Chemical Imaging · Olefin Depolymerization · Olefin Polymerization

[1] R. Geyer, J. R. Jambeck, K. L. Law, *Sci. Adv.* **2017**, *3*, e1700782.
[2] W. Kaminsky, *Macromol. Chem. Phys.* **2008**, *209*, 459–466.
[3] R. Geyer, in *Plast. Waste Recycl*, Elsevier, Amsterdam, **2020**, 13–32.
[4] D. W. Sauter, M. Taoufik, C. Boisson, *Polymer* **2017**, *9*, 185.
[5] J. Qiao, M. Guo, L. Wang, D. Liu, X. Zhang, L. Yu, W. Song, Y. Liu, *Polym. Chem.* **2011**, *2*, 1611–1623.
[6] V. Busico, R. Cipullo, *Prog. Polym. Sci.* **2001**, *26*, 443–533.
[7] W. Kaminsky, *J. Polym. Sci. Part A* **2004**, *42*, 3911–3921.
[8] I. Vollmer, M. J. F. Jenks, M. C. P. Roelands, R. J. White, T. van Harmelen, P. de Wild, G. P. van der Laan, F. Meirer, J. T. F. Keurentjes, B. M. Weckhuysen, *Angew. Chem. Int. Ed.* **2020**, *59*, 15402–15423.
[9] A. J. Martín, C. Mondelli, S. D. Jaydev, J. Pérez-Ramírez, *Chem* **2021**, *7*, 1487–1533.
[10] W. Zhao, S. Hasegawa, J. Fujita, F. Yoshii, T. Sasaki, K. Makuuchi, J. Sun, S. I. Nishimoto, *Polym. Degrad. Stab.* **1996**, *53*, 129–135.
[11] I. Vollmer, M. J. F. Jenks, R. Mayorga González, F. Meirer, B. M. Weckhuysen, *Angew. Chem. Int. Ed.* **2021**, *60*, 16101–16108.
[12] D. Munir, Abdullah, F. Piepenbreier, M. R. Usman, *Powder Technol.* **2017**, *316*, 542–550.
[13] G. Celik, R. M. Kennedy, R. A. Hackler, M. Ferrandon, A. Tennakoon, S. Patnaik, A. M. Lapointe, S. C. Ammal, A. Heyden, F. A. Perras, M. Pruski, S. L. Scott, K. R. Poeppelmeier, A. D. Sadow, D. Massimiliano, *ACS Cent. Sci.* **2019**, *5*, 1795–1803.
[14] A. Tennakoon, X. Wu, A. L. Paterson, S. Patnaik, Y. Pei, A. M. LaPointe, S. C. Ammal, R. A. Hackler, A. Heyden, I. I. Slowing, G. W. Coates, D. Massimiliano, B. Peters, W. Huang, A. D. Sadow, F. A. Perras, *Nat. Catal.* **2020**, *3*, 893–901.
[15] F. Zhang, M. Zeng, R. D. Yappert, J. Sun, Y. H. Lee, A. M. LaPointe, B. Peters, M. M. Abu-Omar, S. L. Scott, *Science* **2020**, *370*, 437–441.

[16] S. Liu, P. A. Kots, B. C. Vance, A. Danielson, D. G. Vlachos, *Sci. Adv.* **2021**, *7*, 8283–8304.
[17] C. Wang, T. Xie, P. A. Kots, B. C. Vance, K. Yu, P. Kumar, J. Fu, S. Liu, G. Tsilomelekis, E. A. Stach, W. Zheng, D. G. Vlachos, *JACS Au* **2021**, *1*, 1422–1434.
[18] C. Jia, S. Xie, W. Zhang, N. N. Intan, J. Sampath, J. Pfaendtner, H. Lin, *Chem Catal.* **2021**, *1*, 437–455.
[19] P. Cossee, *J. Catal.* **1964**, *3*, 80–88.
[20] V. Dufaud, J. M. Basset, *Angew. Chem. Int. Ed.* **1998**, *37*, 806–810.
[21] W. Kaminsky, A. Laban, *Appl. Catal. A* **2001**, *222*, 47–61.
[22] G. W. Coates, Y. D. Y. L. Getzler, *Nat. Rev. Mater.* **2020**, *5*, 501–516.
[23] F. D. Cannavacciuolo, R. Yadav, A. Esper, A. Vittoria, G. Antinucci, F. Zaccaria, R. Cipullo, P. H. M. Budzelaar, V. Busico, G. P. Goryunov, D. V. Uborsky, A. Z. Voskoboynikov, K. Searles, C. Ehm, A. S. Veige, *Angew. Chem. Int. Ed.* **2022**, *61*, e202202258.
[24] R. Miranda, J. Yang, C. Roy, C. Vasile, *Polym. Degrad. Stab.* **2001**, *72*, 469–491.
[25] J. Corker, F. Lefebvre, C. Lécuyer, V. Dufaud, F. Quignard, A. Choplin, J. Evans, J. M. Basset, *Science* **1996**, *271*, 966–969.
[26] W. Kaminsky, F. Hartmann, *Angew. Chem. Int. Ed.* **2000**, *39*, 331–333.
[27] T. F. L. McKenna, A. Di Martino, G. Weickert, J. B. P. Soares, *Macromol. React. Eng.* **2010**, *4*, 40–64.
[28] A. Alizadeh, T. F. L. McKenna, *Macromol. React. Eng.* **2018**, *12*, 1700027.
[29] M. E. Z. Velthoen, J. D. Meeldijk, F. Meirer, B. M. Weckhuysen, *Chem. Eur. J.* **2018**, *24*, 11944–11953.
[30] A. E. Nieuwelink, M. E. Z. Velthoen, Y. C. M. Nederstigt, K. L. Jagtenberg, F. Meirer, B. M. Weckhuysen, *Chem. Eur. J.* **2020**, *26*, 8546–8554.
[31] M. J. Werny, R. Valadian, L. M. Lohse, A.-L. Robisch, S. Zanoni, C. Hendriksen, B. M. Weckhuysen, F. Meirer, *Chem Catal.* **2021**, *1*, 1413–1426.
[32] J. R. Severn, J. C. Chadwick, R. Duchateau, N. Friederichs, *Chem. Rev.* **2005**, *105*, 4073–4147.
[33] G. Fink, B. Steinmetz, J. Zechlin, C. Przybyla, B. Tesche, *Chem. Rev.* **2000**, *100*, 1377–1390.
[34] G. Fink, B. Tesche, F. Korber, S. Knoke, *Macromol. Symp.* **2001**, *173*, 77–87.
[35] B. Horáčková, Z. Grof, J. Kosek, *Chem. Eng. Sci.* **2007**, *62*, 5264–5270.
[36] F. Machado, E. L. Lima, J. C. Pinto, T. F. McKenna, *Polym. Eng. Sci.* **2011**, *51*, 302–310.
[37] K. W. Bossers, R. Valadian, S. Zanoni, R. Smeets, N. Friederichs, J. Garrevoet, F. Meirer, B. M. Weckhuysen, *J. Am. Chem. Soc.* **2020**, *142*, 3691–3695.
[38] a) M. J. Werny, J. Zarupski, I. C. ten Have, A. Piovano, C. Hendriksen, N. H. Friederichs, F. Meirer, E. Groppo, B. M. Weckhuysen, *JACS Au* **2021**, *1*, 1996–2008; b) M. J. Werny, J. Zarupski, I. C. ten Have, A. Piovano, C. Hendriksen, N. H. Friederichs, F. Meirer, E. Groppo, B. M. Weckhuysen, *JACS Au* **2023**, *1*, 2333–2334.
[39] M. Ahsan Bashir, T. F. L. McKenna, *Polym. React. Eng. Dispersed Syst. Vol. I*, Springer International Publishing, **2018**, 19–63.
[40] P. Kittilsen, T. F. McKenna, H. Svendsen, H. A. Jakobsen, S. B. Fredriksen, *Chem. Eng. Sci.* **2001**, *56*, 4015–4028.
[41] J. T. M. Pater, G. Weickert, J. Loos, W. P. M. van Swaaij, *Chem. Eng. Sci.* **2001**, *56*, 4107–4120.
[42] J. M. Zhou, N. H. Li, N. Y. Bu, D. T. Lynch, S. E. Wanke, *J. Appl. Polym. Sci.* **2003**, *90*, 1319–1330.
[43] S. Knoke, F. Korber, G. Fink, B. Tesche, *Macromol. Chem. Phys.* **2003**, *204*, 607–617.
[44] H. Hammawa, S. E. Wanke, *Polym. Int.* **2006**, *55*, 426–434.
[45] X. Zheng, J. Loos, *Macromol. Symp.* **2006**, *236*, 249–258.
[46] K. W. Bossers, L. D. B. Mandemaker, N. Nikolopoulos, Y. Liu, M. Rohnke, P. de Peinder, B. J. P. Terlingen, F. Walther, J. M. Dorresteijn, T. Hartman, B. M. Weckhuysen, *Nat. Commun.* **2022**, *13*, 4954.
[47] S. Zanoni, N. Nikolopoulos, A. Welle, A. Vantomme, B. M. Weckhuysen, *Catal. Sci. Technol.* **2021**, *11*, 5335–5348.
[48] M. J. Werny, D. Müller, C. Hendriksen, R. Chan, N. H. Friederichs, C. Fella, F. Meirer, B. M. Weckhuysen, *ChemCatChem* **2023**, *14*, e202200067.
[49] a) S. Zanoni, N. Nikolopoulos, A. Welle, V. Cirriez, B. M. Weckhuysen, *ChemCatChem* **2023**, *15*, e202300222; b) S. Zanoni, Characterization of Supported Metallocene Catalysts for Ethylene Polymerization, PhD Thesis, Utrecht University, **2023**.
[50] X. Zheng, M. Smit, J. C. Chadwick, J. Loos, *Macromolecules* **2005**, *38*, 4673–4678.
[51] H. L. Rönkkö, T. Korpela, H. Knuuttila, T. T. Pakkanen, P. Denifl, T. Leinonen, M. Kemell, M. Leskelä, *J. Mol. Catal. A* **2009**, *309*, 40–49.
[52] D. Tran, C. S. Sowah, K. Y. Choi, *Macromolecules* **2022**, *55*, 2444–2455.
[53] J. D. Grunwaldt, C. G. Schroer, *Chem. Soc. Rev.* **2010**, *39*, 4741–4753.
[54] F. Meirer, B. M. Weckhuysen, *Nat. Rev. Mater.* **2018**, *3*, 324–340.
[55] W. Curtis Conner, S. W. Webb, P. Spanne, K. W. Jones, *Macromolecules* **1990**, *23*, 4742–4747.
[56] K. W. Jones, P. Spanne, S. W. Webb, W. C. Conner, R. A. Beyerlein, W. J. Reagan, F. M. Dautzenberg, *Nucl. Inst. Methods Phys. Res. B* **1991**, *56–57*, 427–432.
[57] K. W. Jones, P. Spanne, W. B. Lindquist, W. C. Conner, M. Ferrero, *Nucl. Inst. Methods Phys. Res. B* **1992**, *68*, 105–110.
[58] M. A. Ferrero, R. Sommer, P. Spanne, K. W. Jones, W. C. Conner, *J. Polym. Sci. Part A* **1993**, *31*, 2507–2512.
[59] D. Cicmil, J. Meeuwissen, A. Vantomme, J. Wang, I. K. van Ravenhorst, H. E. van Der Bij, A. Muñoz-Murillo, B. M. Weckhuysen, *Angew. Chem. Int. Ed.* **2015**, *54*, 13073–13079.
[60] M. K. Jongkind, F. Meirer, K. W. Bossers, I. C. ten Have, H. Ohldag, B. Watts, T. van Kessel, N. Friederichs, B. M. Weckhuysen, *Chem. Eur. J.* **2021**, *27*, 1688–1699.
[61] M. Arakawa, M. Kishimoto, Y. Nakanishi, K. Mita, M. Takenaka, *Polym. J.* **2022**, *54*, 243–248.
[62] F. Pfeiffer, *Nat. Photonics* **2018**, *12*, 9–17.
[63] K. W. Bossers, R. Valadian, J. Garrevoet, S. van Malderen, R. Chan, N. Friederichs, J. Severn, A. Wilbers, S. Zanoni, M. K. Jongkind, B. M. Weckhuysen, F. Meirer, *JACS Au* **2021**, *1*, 852–864.
[64] L. Seda, A. Zubov, M. Bobak, J. Kosek, A. Kantzas, *Macromol. React. Eng.* **2008**, *2*, 495–512.
[65] J. B. P. Soares, T. F. L. McKenna, *Polyolefin Reaction Engineering*, Wiley-VCH, Weinheim, **2012**.
[66] L. Meisterová, A. Zubov, K. Smolná, F. Štěpánek, J. Kosek, *Macromol. React. Eng.* **2013**, *7*, 277–288.
[67] H. Coceancigh, D. A. Higgins, T. Ito, *Anal. Chem.* **2019**, *91*, 405–424.
[68] N. M. Esfandiari, S. A. Blum, *J. Am. Chem. Soc.* **2011**, *133*, 18145–18147.
[69] T. Cordes, S. A. Blum, *Nat. Chem.* **2013**, *5*, 993–999.
[70] Q. T. Easter, S. A. Blum, *Angew. Chem. Int. Ed.* **2017**, *56*, 13772–13775.
[71] C. Liu, K. Kubo, E. Wang, K. S. Han, F. Yang, G. Chen, F. A. Escobedo, G. W. Coates, P. Chen, *Science* **2017**, *358*, 352–355.
[72] C. Liu, S. Baral, K. Gu, X. Mao, P. Chen, *Trends Chem.* **2021**, *3*, 318–331.
[73] J. T. M. Pater, G. Weickert, W. P. M. van Swaaij, *Chimia* **2001**, *55*, 231–233.

[74] V. P. Oleshko, P. A. Crozier, R. D. Cantrell, A. D. Westwood, *Macromol. Rapid Commun.* **2001**, *22*, 34–40.
[75] K. Zöllner, K. H. Reichert, *Chem. Eng. Sci.* **2001**, *56*, 4099–4106.
[76] K. Zöllner, K. H. Reichert, *Chem. Eng. Technol.* **2002**, *25*, 707–710.
[77] S. Knoke, D. Ferrari, B. Tesche, G. Fink, *Angew. Chem. Int. Ed.* **2003**, *42*, 5090–5093.
[78] M. Abboud, K. Kallio, K. H. Reichert, *Chem. Eng. Technol.* **2004**, *27*, 694–698.
[79] D. Ferrari, G. Fink, *Macromol. Mater. Eng.* **2005**, *290*, 1125–1136.
[80] J. T. M. Pater, G. Weickert, W. P. M. van Swaaij, *AIChE J.* **2003**, *49*, 450–464.
[81] R. Xalter, R. Mülhaupt, *Macromol. React. Eng.* **2010**, *4*, 25–39.
[82] Y. Jang, K. Bieber, C. Naundorf, N. Nenov, M. Klapper, K. Müllen, D. Ferrari, S. Knoke, G. Fink, *e-Polymers* **2005**. https://doi.org/10.1515/epoly.2005.5.1.132
[83] Y. J. Jang, C. Naundorf, M. Klapper, K. Müllen, *Macromol. Chem. Phys.* **2005**, *206*, 2027–2037.
[84] M. Klapper, D. Joe, S. Nietzel, J. W. Krumpfer, K. Müllen, *Chem. Mater.* **2014**, *26*, 802–819.
[85] R. Dorresteijn, S. Nietzel, D. Joe, Y. Gerkmann, G. Fink, M. Klapper, K. Müllen, *J. Polym. Sci. Part A* **2014**, *52*, 450–459.
[86] M. Stork, A. Herrmann, T. Nemnich, M. Klapper, K. Müllen, *Angew. Chem. Int. Ed.* **2000**, *39*, 4367–4369.
[87] M. J. Werny, K. B. Siebers, N. H. Friederichs, C. Hendriksen, F. Meirer, B. M. Weckhuysen, *J. Am. Chem. Soc.* **2022**, *144*, 21287–21294.
[88] J. J. Janimak, L. Markey, G. C. Stevens, *Polymer* **2001**, *42*, 4675–4685.
[89] I. L. Hosier, R. G. Alamo, J. S. Lin, *Polymer* **2004**, *45*, 3441–3455.
[90] R. Pellecchia, P. Shutov, J. Wang, M. Gahleitner, *Macromol. React. Eng.* **2020**, *14*, 2000022.
[91] A. Dazzi, C. B. Prater, Q. Hu, D. B. Chase, J. F. Rabolt, C. Marcott, *Appl. Spectrosc.* **2012**, *66*, 1365–1384.
[92] F. Tang, P. Bao, Z. Su, *Anal. Chem.* **2016**, *88*, 4926–4930.
[93] P. Nguyen-Tri, P. Ghassemi, P. Carriere, S. Nanda, A. A. Assadi, D. D. Nguyen, *Polymer* **2020**, *12*, 1142.
[94] D. Nowak, W. Morrison, H. K. Wickramasinghe, J. Jahng, E. Potma, L. Wan, R. Ruiz, T. R. Albrecht, K. Schmidt, J. Frommer, D. P. Sanders, S. Park, *Sci. Adv.* **2016**, *2*, e1501571.
[95] K. L. Gu, Y. Zhou, W. A. Morrison, K. Park, S. Park, Z. Bao, *ACS Nano* **2018**, *12*, 1473–1481.
[96] C. Sun, F. Pan, H. Bin, J. Zhang, L. Xue, B. Qiu, Z. Wei, Z. G. Zhang, Y. Li, *Nat. Commun.* **2018**, *9*, 743.
[97] V. J. Ruddick, J. P. S. Badyal, *J. Phys. Chem. B* **1997**, *101*, 1791–1793.
[98] T. J. Young, M. A. Monclus, T. L. Burnett, W. R. Broughton, S. L. Ogin, P. A. Smith, *Meas. Sci. Technol.* **2011**, *22*, 125703.
[99] F. Cavalieri, F. Padella, *Waste Manage.* **2002**, *22*, 913–916.
[100] V. Štrukil, *ChemSusChem* **2021**, *14*, 330–338.
[101] V. P. Balema, I. Z. Hlova, S. L. Carnahan, M. Seyedi, O. Dolotko, A. J. Rossini, I. Luzinov, *New J. Chem.* **2021**, *45*, 2935–2938.
[102] M. Veselý, R. Valadian, L. Merten Lohse, M. Toepperwien, K. Spiers, J. Garrevoet, E. T. C. Vogt, T. Salditt, B. M. Weckhuysen, F. Meirer, *ChemCatChem* **2021**, *13*, 2494–2507.
[103] S. Weber, D. Batey, S. Cipiccia, M. Stehle, K. L. Abel, R. Gläser, T. L. Sheppard, *Angew. Chem. Int. Ed.* **2021**, *60*, 21772–21777.
[104] F. Meirer, S. Kalirai, D. Morris, S. Soparawalla, Y. Liu, G. Mesu, J. C. Andrews, B. M. Weckhuysen, *Sci. Adv.* **2015**, *1*, e1400199.
[105] S. Kalirai, U. Boesenberg, G. Falkenberg, F. Meirer, B. M. Weckhuysen, *ChemCatChem* **2015**, *7*, 3674–3682.
[106] J. Ihli, R. R. Jacob, M. Holler, M. Guizar-Sicairos, A. Diaz, J. C. Da Silva, D. Ferreira Sanchez, F. Krumeich, D. Grolimund, M. Taddei, W. C. Cheng, Y. Shu, A. Menzel, J. A. van Bokhoven, *Nat. Commun.* **2017**, *8*, 809.
[107] J. Ihli, D. Ferreira Sanchez, R. R. Jacob, V. Cuartero, O. Mathon, F. Krumeich, C. Borca, T. Huthwelker, W. C. Cheng, Y. Y. Shu, S. Pascarelli, D. Grolimund, A. Menzel, J. A. van Bokhoven, *Angew. Chem. Int. Ed.* **2017**, *56*, 14031–14035.
[108] M. Gambino, M. Veselý, M. Filez, R. Oord, D. Ferreira Sanchez, D. Grolimund, N. Nesterenko, D. Minoux, M. Maquet, F. Meirer, B. M. Weckhuysen, *Angew. Chem. Int. Ed.* **2020**, *59*, 3922–3927.
[109] I. L. C. Buurmans, J. Ruiz-Martínez, W. V. Knowles, D. van Der Beek, J. A. Bergwerff, E. T. C. Vogt, B. M. Weckhuysen, *Nat. Chem.* **2011**, *3*, 862–867.
[110] M. M. Kerssens, A. Wilbers, J. Kramer, P. De Peinder, G. Mesu, B. J. Nelissen, E. T. C. Vogt, B. M. Weckhuysen, *Faraday Discuss.* **2016**, *188*, 69–79.
[111] A.-E. Nieuwelink, J. C. Vollenbroek, R. M. Tiggelaar, J. G. Bomer, A. van den Berg, M. Odijk, B. M. Weckhuysen, *Nat. Catal.* **2021**, *4*, 1070–1079.
[112] A. M. Beale, S. D. M. Jacques, B. M. Weckhuysen, *Chem. Soc. Rev.* **2010**, *39*, 4656–4672.
[113] J. N. Weker, X. Huang, M. F. Toney, *Curr. Opin. Chem. Eng.* **2016**, *12*, 14–21.
[114] E. De Smit, I. Swart, J. F. Creemer, G. H. Hoveling, M. K. Gilles, T. Tyliszczak, P. J. Kooyman, H. W. Zandbergen, C. Morin, B. M. Weckhuysen, F. M. F. de Groot, *Nature* **2008**, *456*, 222–225.
[115] F. M. F. de Groot, E. de Smit, M. M. van Schooneveld, L. R. Aramburo, B. M. Weckhuysen, *ChemPhysChem* **2010**, *11*, 951–962.
[116] I. K. van Ravenhorst, C. Vogt, H. Oosterbeek, K. W. Bossers, J. G. Moya-Cancino, A. P. van Bavel, A. M. J. van der Eerden, D. Vine, F. M. F. de Groot, F. Meirer, B. M. Weckhuysen, *Angew. Chem. Int. Ed.* **2018**, *57*, 11957–11962.
[117] Y. Fam, T. L. Sheppard, J. Becher, D. Scherhaufer, H. Lambach, S. Kulkarni, T. F. Keller, A. Wittstock, F. Wittwer, M. Seyrich, D. Brueckner, M. Kahnt, X. Yang, A. Schropp, A. Stierle, C. G. Schroer, J. D. Grunwaldt, *J. Synchrotron Radiat.* **2019**, *26*, 1769–1781.
[118] S. W. T. Price, K. Geraki, K. Ignatyev, P. T. Witte, A. M. Beale, J. F. W. Mosselmans, *Angew. Chem. Int. Ed.* **2015**, *54*, 9886–9889.
[119] T. L. Sheppard, S. W. T. Price, F. Benzi, S. Baier, M. Klumpp, R. Dittmeyer, W. Schwieger, J. D. Grunwaldt, *J. Am. Chem. Soc.* **2017**, *139*, 7855–7863.
[120] I. D. Gonzalez-Jimenez, K. Cats, T. Davidian, M. Ruitenbeek, F. Meirer, Y. Liu, J. Nelson, J. C. Andrews, P. Pianetta, F. M. F. de Groot, B. M. Weckhuysen, *Angew. Chem. Int. Ed.* **2012**, *51*, 11986–11990.
[121] K. H. Cats, I. D. Gonzalez-Jimenez, Y. Liu, J. Nelson, D. van Campen, F. Meirer, A. M. J. van Der Eerden, F. M. F. de Groot, J. C. Andrews, B. M. Weckhuysen, *Chem. Commun.* **2013**, *49*, 4622–4624.
[122] K. H. Cats, J. C. Andrews, O. Stéphan, K. March, C. Karunakaran, F. Meirer, F. M. F. de Groot, B. M. Weckhuysen, *Catal. Sci. Technol.* **2016**, *6*, 4438–4449.
[123] J. C. Andrews, B. M. Weckhuysen, *ChemPhysChem* **2013**, *14*, 3655–3666.
[124] A. Vamvakeros, S. D. M. Jacques, V. Middelkoop, M. Di Michiel, C. K. Egan, I. Z. Ismagilov, G. B. M. Vaughan, F. Gallucci, M. van Sint Annaland, P. R. Shearing, R. J. Cernik, A. M. Beale, *Chem. Commun.* **2015**, *51*, 12752–12755.

[125] S. W. T. Price, D. J. Martin, A. D. Parsons, W. A. Sławiński, A. Vamvakeros, S. J. Keylock, A. M. Beale, J. F. W. Mosselmans, *Sci. Adv.* **2017**, *3*, e1602838.
[126] P. Senecal, S. D. M. Jacques, M. Di Michiel, S. A. J. Kimber, A. Vamvakeros, Y. Odarchenko, I. Lezcano-Gonzalez, J. Paterson, E. Ferguson, A. M. Beale, *ACS Catal.* **2017**, *7*, 2284–2293.
[127] A. Vamvakeros, S. D. M. Jacques, M. Di Michiel, D. Matras, V. Middelkoop, I. Z. Ismagilov, E. V. Matus, V. V. Kuznetsov, J. Drnec, P. Senecal, A. M. Beale, *Nat. Commun.* **2018**, *9*, 4751.
[128] D. Matras, A. Vamvakeros, S. D. M. Jacques, M. Di Michiel, V. Middelkoop, I. Z. Ismagilov, E. V. Matus, V. V. Kuznetsov, R. J. Cernik, A. M. Beale, *J. Mater. Chem. A* **2021**, *9*, 11331–11346.
[129] I. J. Drake, T. C. N. Liu, M. Gilles, T. Tyliszczak, A. L. D. Kilcoyne, D. K. Shuh, R. A. Mathies, A. T. Bell, *Rev. Sci. Instrum.* **2004**, *75*, 3242–3247.
[130] M. Holler, T. Aidukas, L. Heller, C. Appel, N. W. Phillips, E. Müller-Gubler, M. Guizar-Sicairos, J. Raabe, J. Ihli, S. Svensson, *J. Synchrotron Radiat.* **2022**, *29*, 1223–1231.
[131] G. Martinez-Criado, J. Villanova, R. Tucoulou, D. Salomon, J. P. Suuronen, S. Laboure, C. Guilloud, V. Valls, R. Barrett, E. Gagliardini, Y. Dabin, R. Baker, S. Bohic, C. Cohen, J. Morse, *Synchrotron Radiat.* **2016**, *23*, 344–352.
[132] J. Villanova, R. Kumar, R. Daudin, P. Lhuissier, D. Jauffres, C. L. Martin, R. Tucoulou, S. Laboure, G. Martinez-Criado, L. Salvo, *Microsc. Microanal.* **2018**, *24*, 450–451.
[133] V. Vanpeene, J. Villanova, A. King, B. Lestriez, E. Maire, L. Roué, *Adv. Energy Mater.* **2019**, *9*, 1803947.
[134] P. Raimondi, *Synchrotron Radiat. News* **2016**, *29*, 8–15.
[135] R. Röhlsberger, C. G. Schroer, R. Wanzenberg, S. Klumpp, W. Wurth, *Synchrotron Radiat. News* **2019**, *32*, 27–31.
[136] A. Rack, *Synchrotron Radiat. News* **2020**, *33*, 20–28.
[137] T. F. McKenna, J. B. P. Soares, *Chem. Eng. Sci.* **2001**, *56*, 3931–3949.
[138] C. E. Cardenas, J. Yang, B. M. Anderson, L. E. Court, K. B. Brock, *Semin. Radiat. Oncol.* **2019**, *29*, 185–197.
[139] J. J. Bailey, J. Chen, J. Hack, M. Perez-Page, S. M. Holmes, D. J. L. Brett, P. R. Shearing, *J. Power Sources* **2021**, *509*, 230347.
[140] A. D. Shum, C. P. Liu, W. H. Lim, D. Y. Parkinson, I. V. Zenyuk, *Transp. Porous Media* **2022**, *144*, 715–737.
[141] K. Tang, Q. Meyer, R. White, R. T. Armstrong, P. Mostaghimi, Y. Da Wang, S. Liu, C. Zhao, K. Regenauer-Lieb, P. K. M. Tung, *Comput. Chem. Eng.* **2022**, *161*, 107768.
[142] P. C. Thüne, J. Loos, P. J. Lemstra, J. W. Niemantsverdriet, *J. Catal.* **1999**, *183*, 1–5.
[143] S. H. Kim, G. A. Somorjai, *J. Phys. Chem. B* **2001**, *105*, 3922–3927.
[144] P. C. Thüne, J. Loos, U. Weingarten, F. Müller, W. Kretschmer, W. Kaminsky, P. J. Lemstra, H. Niemantsverdriet, *Macromolecules* **2003**, *36*, 1440–1445.
[145] A. Andoni, J. C. Chadwick, S. Milani, H. J. W. Niemantsverdriet, P. C. Thüne, *J. Catal.* **2007**, *247*, 129–136.
[146] A. Andoni, J. C. Chadwick, H. J. W. Niemantsverdriet, P. C. Thüne, *Macromol. Symp.* **2007**, *260*, 140–146.
[147] S. Y. Lee, S. K. Kim, T. M. Nguyen, J. S. Chung, S. B. Lee, K. Y. Choi, *Macromolecules* **2011**, *44*, 1385–1392.
[148] S. Y. Lee, K. Y. Choi, *Macromol. React. Eng.* **2014**, *8*, 755–765.
[149] M. Solsona, A. E. Nieuwelink, F. Meirer, L. Abelmann, M. Odijk, W. Olthuis, B. M. Weckhuysen, A. van den Berg, *Angew. Chem. Int. Ed.* **2018**, *57*, 10589–10594.
[150] R. G. Geitenbeek, A. E. Nieuwelink, T. S. Jacobs, B. B. V. Salzmann, J. Goetze, A. Meijerink, B. M. Weckhuysen, *ACS Catal.* **2018**, *8*, 2397–2401.
[151] T. Hartman, R. G. Geitenbeek, G. T. Whiting, B. M. Weckhuysen, *Nat. Catal.* **2019**, *2*, 986–996.
[152] T. Hartman, R. G. Geitenbeek, C. S. Wondergem, W. van Der Stam, B. M. Weckhuysen, *ACS Nano* **2020**, *14*, 3725–3735.
[153] T. P. van Swieten, T. van Omme, D. J. van Den Heuvel, S. J. W. Vonk, R. G. Spruit, F. Meirer, H. H. P. Garza, B. M. Weckhuysen, A. Meijerink, F. T. Rabouw, R. G. Geitenbeek, *ACS Appl. Nano Mater.* **2021**, *4*, 4208–4215.
[154] Y. Yao, Y. Jiang, J. A. Klug, M. Wojcik, E. R. Maxey, N. S. Sirica, C. Roehrig, Z. Cai, S. Vogt, B. Lai, J. Deng, *Sci. Rep.* **2020**, *10*, 19550.
[155] F. Wittwer, M. Lyubomirskiy, F. Koch, M. Kahnt, M. Seyrich, J. Garrevoet, C. David, C. G. Schroer, *Appl. Phys. Lett.* **2021**, *118*, 171102.
[156] M. Lyubomirskiy, F. Wittwer, M. Kahnt, F. Koch, A. Kubec, K. V. Falch, J. Garrevoet, M. Seyrich, C. David, C. G. Schroer, *Sci. Rep.* **2022**, *12*, 6203.
[157] S. Rejman, I. Vollmer, M. J. Werny, E. T. C. Vogt, F. Meirer, B. M. Weckhuysen, *Chem. Sci.* **2023**, *14*, 10068–10080.

Manuscript received: April 29, 2023
Accepted manuscript online: October 2, 2023
Version of record online: November 21, 2023